



## TABLE OF CONTENTS

<u>Section</u>	<u>Title</u>	<u>Page</u>
I	INTRODUCTION	1
II	SUMMARY OF TECHNICAL WORK PERFORMED FOR THE PERIOD 1 SEPTEMBER 1969 THROUGH 24 NOVEMBER 1969	3
III	TECHNICAL PAPERS PRESENTED AT SCIENTIFIC AND/OR PROFESSIONAL MEETINGS	96
IV	QUARTERLY PROGRESS REPORT FOR HOURS WORKED IN THE PERIOD 1 SEPTEMBER 1969 THROUGH 24 NOVEMBER 1969	97
	REFERENCES	98

## I. INTRODUCTION

This sixth Quarterly Progress Report describes the technical progress achieved from 1 September 1969 through 24 November 1969 under NASA contract No. NASw-1726. Scientific investigation accomplished during this reporting period resulted in the generation of the following papers submitted, accepted and/or published in accredited scientific journals.

### Technical Papers Submitted, Accepted and/or Published

#### a. Accepted:

$\text{CO}_2^+$  Dayglow on Mars and Venus  
(A. Dalgarno & T. Degges)

Proc. I.A.U.  
Symposium 40 on  
Planetary Atmospheres  
Marfa, Texas (10/27/69)

Angular Distribution of Photoelectrons and Partial Photoionization Cross Sections (J. A. R. Samson)

Proc. Roy. Soc.

Carbon Atoms in the Upper Atmosphere of Venus (F. Marmo and A. Engelman)

ICARUS

Photon Scattering by Argon in the VUV  
(R. Cairns, F. Marmo & J. Samson)

J. Opt. Soc. Am.

#### b. Published:

Electronic States of  $\text{C}_6\text{H}_6^+$  (J. Samson)

Chem. Phys. Letters  
4, 257 (1969).

Line Broadening in Photoelectron Spectroscopy (J. Samson)

Rev. Sci. Instr.  
40, 1174 (1969).

On the Measurement of Rayleigh Scattering (J. Samson)

J. Quant. Spectrosc.  
& Radiat. Trans. 9,  
875 (1969)

#### Technical Papers Presented at Scientific or Professional Meetings

"Angular Distributions of Photoelectrons and Partial Photoionization Cross Sections," by James A. R. Samson; paper delivered at the First Annual Meeting of the Division of Electron and Atomic Physics of the American Physical Society on 17-19 November 1969 in Madison, Wisconsin.

In Section II, technical summaries are presented on the work performed during the current reporting period. Section III contains brief summaries of technical papers presented at scientific and/or professional meetings as well as other miscellaneous topics of interest in the performance of the current contract commitments. Finally, in compliance with the requirements of the contract, an integrated tabulation by labor category and grade of total hours expended in the execution of the contract, for the specified reported time interval is included in Section IV.

## II. SUMMARY OF TECHNICAL WORK PERFORMED FOR THE PERIOD 1 SEPTEMBER 1969 THROUGH 24 NOVEMBER 1969

The technical progress accomplished during the current reporting period can be conveniently described in terms of the two major categories contained in the statement of work: (A) laboratory studies, and (B) theoretical studies.

### A. LABORATORY STUDIES

During the current quarterly reporting period a number of laboratory studies were performed in accordance with the tasks specified in the subject work statement. Specifically, the electronic states of  $C_6H_6^+$ , photon scattering by argon in the VUV, yield of ions resulting from photoionization, measurement of ionic mobilities, which are discussed below in the indicated order.

#### 1. The Electronic States of $C_6H_6^+$

Photoelectron spectroscopy is an ideal tool for determining the ionization potentials of atoms and molecules. The technique further gives an insight into the bonding nature of the electrons. In the case of benzene, photoelectron spectroscopy using the  $584\text{\AA}$  resonance line of He I gives 9.25 and 11.5 eV as the two lowest ionization energies of the molecule. <sup>(1,3)</sup> These values are in agreement with the Rydberg analysis of the vacuum ultraviolet absorption spectrum of benzene. <sup>(4,5)</sup> These two ionization potentials have been attributed to the removal of a  $\pi$  electron. <sup>(3,5)</sup> However, theory has predicted that two sigma orbitals should lie between the two lowest  $\pi$  orbitals. <sup>(6-9)</sup> This has led to ex-

periments in search for ionization potentials lying between 9.25 and 11.5 eV. Momigny, et al.<sup>(10)</sup> have used photoionization techniques and measured the number of ions produced per incident photon, that is, a quantity proportional to the photoionization cross section. Natalis, et al.<sup>(11)</sup> have studied the photoelectron spectrum of benzene using undispersed light sources of He (584Å), Ne (736, 744Å), and Ar (1048, 1067Å). Peatman, et al.<sup>(12)</sup> have studied this region using a photoionization resonance technique. This technique detects zero kinetic energy electrons as a function of photon energy. These experiments have all suggested the existence of two electronic states of benzene in the vicinity of 10.35 and 10.85 eV. Baker, et al.<sup>(13)</sup> also using undispersed radiation, have presented data illustrating the absence of structure except that which can be accounted for by impurity lines present in the light source. It is the purpose of this note to explain these results and to present photoelectron spectroscopy data at various wavelengths showing that the first two electronic states of the benzene ion lie at 9.25 and 11.5 eV.

Photoionization measurements have been very successful in identifying first ionization potentials.<sup>(14,15)</sup> However, higher ionization potentials obtained by this technique must be considered doubtful. The reason is that unresolved autoionizing structure can give a step in the ionization curve which is then erroneously considered a higher ionization potential. Partial resolution of this structure still gives the

appearance of an underlying continuum. Complete resolution can reveal the true nature of the phenomenon except when the usually diffuse autoionizing lines overlap. Previously reported photoionization studies of benzene, with or without mass analysis, have used band widths between 1 and 3 Å. (10,16-19) Under poor resolution steps occur at 10.35 and 10.85 eV which is just the onset potential of two major groups of autoionizing lines. As the resolution improves the step function nature of the photoionization cross section curve in the 10 to 11 eV region disappears revealing the autoionizing structure.

In the photoionization resonance experiment zero kinetic energy electrons are observed at 10.385 and 10.471 eV. This result can also be explained by autoionization. Direct ionization at photon energies above an ionization threshold will produce non-zero energy electrons and hence no peaks will be observed. However, when an autoionizing transition occurs various vibrational states of the ion are populated. (20,21) The degree of population can be expected to depend on the overlap integrals between the autoionizing state and the particular electronic state of the ion involved. A finite probability exists that a transition will be made into a vibrational level of the ion coinciding with the autoionizing state and hence zero energy electrons will appear. In the particular case of benzene, autoionizing states are observed at 1193.2 Å (10.39 eV), 1184.2 Å

(10.470 eV), and  $1181.2\text{\AA}$  (10.498 eV).<sup>(22)</sup> Within the accuracy of these measurements ( $\pm 0.004$  eV) the first two autoionizing levels agree precisely with the peaks observed in the photoionization resonance experiment. The fact that the peaks are extremely weak indicates a low probability for producing zero energy electrons with these particular autoionizing states. Nevertheless, photoionization resonance experiments are subject to the uncertainties produced by autoionizing transitions.

The photoelectron spectrum of benzene obtained with the  $584\text{\AA}$  He I line shows no structure between 9.25 and 11.5 eV.<sup>(1,2,11)</sup> However, as suggested by Momigny and Lorquet,<sup>(23)</sup> it is possible that all the ionization cross sections for the levels at 10.35 and 10.85 eV are too low to be observed at  $584\text{\AA}$  and can only be detected nearer threshold. In fact, photoelectron spectroscopy data by Vilesov and Akopyan<sup>(24)</sup> show some anomalous peaks using monochromatic radiation between 10 and 11 eV. From this data it would appear that an electronic state exists at about 10.75 eV. However, in their own analysis Vilesov states that the autoionizing structure probably is responsible for their observed anomalies.<sup>(17,24)</sup>

Natalis, et al.<sup>(11)</sup> have investigated the photoelectron spectrum of benzene using undispersed resonance radiation from argon ( $1048\text{-}1067\text{\AA}$ ), neon ( $736\text{-}744\text{\AA}$ ) and helium ( $584\text{\AA}$ ) light sources. In the region of 10-11 eV peaks were observed in the photoelectron spectrum at 9.99 and 10.67 eV with the argon source, while one peak was observed at 10.90 eV when the neon source was used. No peaks were observed when the helium light source



was used. Natalis, et al. feel that within the accuracy of their experiment the 10.67 eV peak and the 10.90 eV peak refer to the same energy level. These observed peaks can be explained by the presence of impurity lines in the light sources. The most frequently observed impurity lines in this wavelength region are  $1215.7\text{\AA}$  H I (10.20 eV),  $1200.2\text{\AA}$  N I (10.33 eV), and  $1135.0\text{\AA}$  N I (10.93 eV).<sup>(25)</sup> These lines would give rise to apparent energy levels in benzene at 10.78, 10.65 and 10.04 eV, respectively, when the argon light source was used (computed using the average energy of the two argon resonance lines). The first two impurity lines would account for the observed level at 10.67 eV while the third impurity line accounts for their observed level at 9.99 eV.

With the neon light source the  $736\text{\AA}$  resonance line is the most intense. The impurity lines in this case would give rise to apparent energy levels at 15.90, 15.77, and 15.17 eV, respectively. The highest energy level reported by Natalis, et al. lies at 15.2 eV which again can be accounted for by the impurity  $1135\text{\AA}$  N I line. These impurity lines cannot account for the apparent level quoted at 10.9 eV. However, this peak is extremely weak and must be questionable when obtained using an undispersed light source and low energy resolution apparatus.

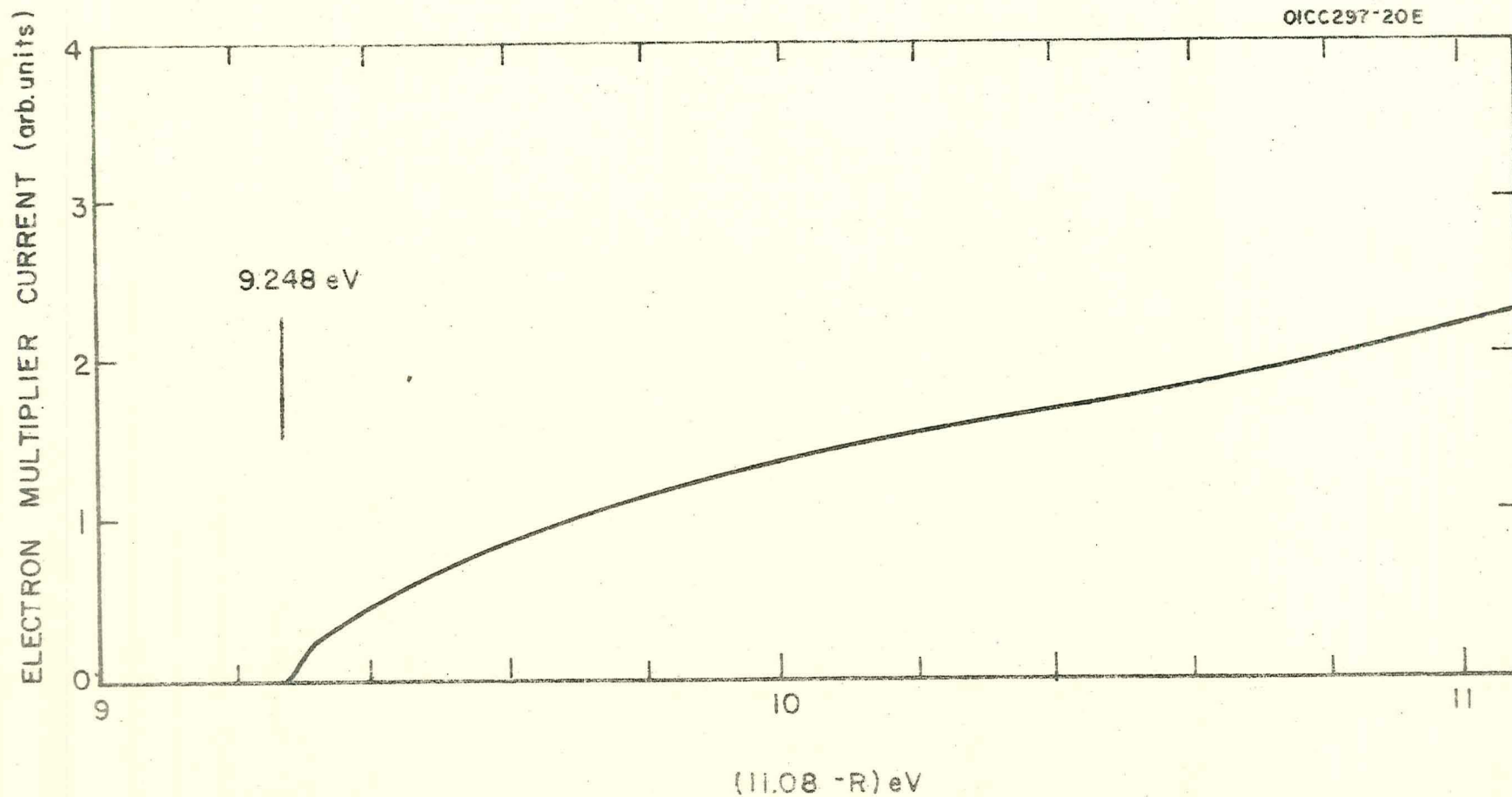
When the helium light source is used, the impurity lines give rise to apparent energy levels at 20.27, 20.14, and 19.54 eV, respectively. The H I impurity level can be observed at 20.26 eV in the spectra reported by Baker, et al.<sup>(13)</sup> and by Clark and Frost.<sup>(2)</sup> The  $1135\text{\AA}$  N I impurity level is also observed in the photoelectron spectrum by Baker, et al.

With care the nitrogen impurity lines can be removed, but it is very difficult to eliminate the hydrogen Lyman alpha line. The problem of impurity lines has been discussed recently with respect to anomalous structure observed in Hg and NO. (26,27) Obviously, care must be exercised in interpreting weak peaks in photoelectron spectra when unpersed radiation is used.

In the present work a vacuum monochromator was used in conjunction with a dc glow discharge to produce monochromatic radiation (halfwidth =  $0.8\text{\AA}$ ). The glow discharge was operated with  $\text{H}_2$ , Ne, Ar, and He gases to produce intense spectral lines in the energy range 9.8 to 21.2 eV. The monochromator was coupled to a spherical retarding potential energy analyzer as described in a previous publication. (28) The analyzer had a resolving power of about 0.8 percent for electron energies in excess of 4 eV. Below 4 eV the half width of a line tended towards a fixed value of about 30 mV.

Data were taken at many wavelengths between 1253 and  $584\text{\AA}$ . Representative data taken at  $1119\text{\AA}$  (11.1 eV),  $1048.2\text{\AA}$  (11.83 eV), and  $735.89\text{\AA}$  (16.85 eV) are reproduced in Figures 1, 2, and 3 respectively. None of the data revealed new states between 9.25 and 11.5 eV. In the figures the higher energy levels were determined with respect to the spectroscopic value of 9.248 eV obtained by Wilkinson. (4)

Although no states were observed within the noise level of the traces it can still be argued that the desired levels have extremely low photoionization cross sections. However, we believe that from the



185

Figure 1:  $1119\text{\AA}$  (11.1 eV) Photoelectron retarding potential curve for benzene. Hydrogen was used in the light source.

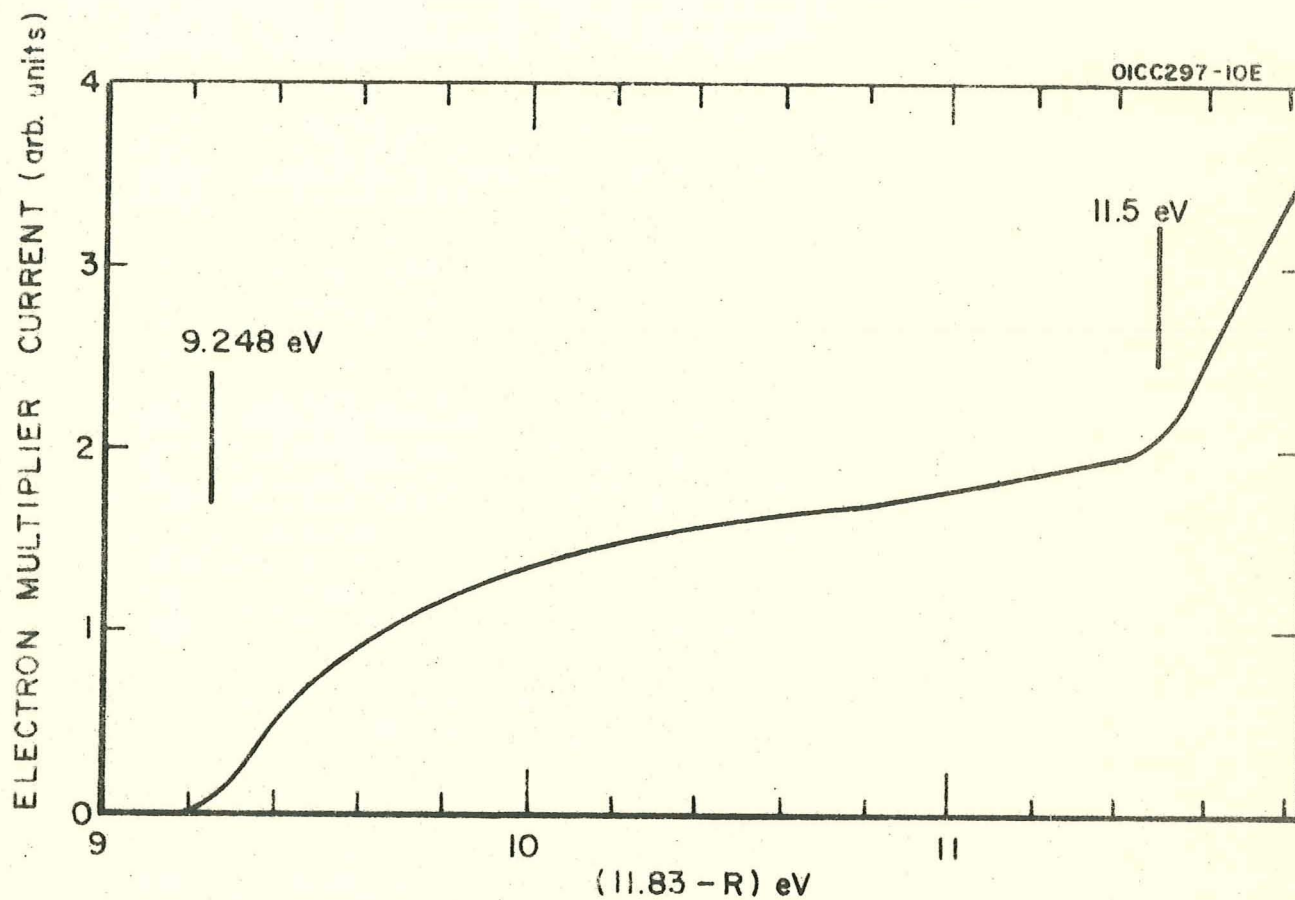


Figure 2:  $1048.2\text{\AA}$  (11.83 eV) Photoelectron retarding potential curve for benzene. Argon was used in the light source.

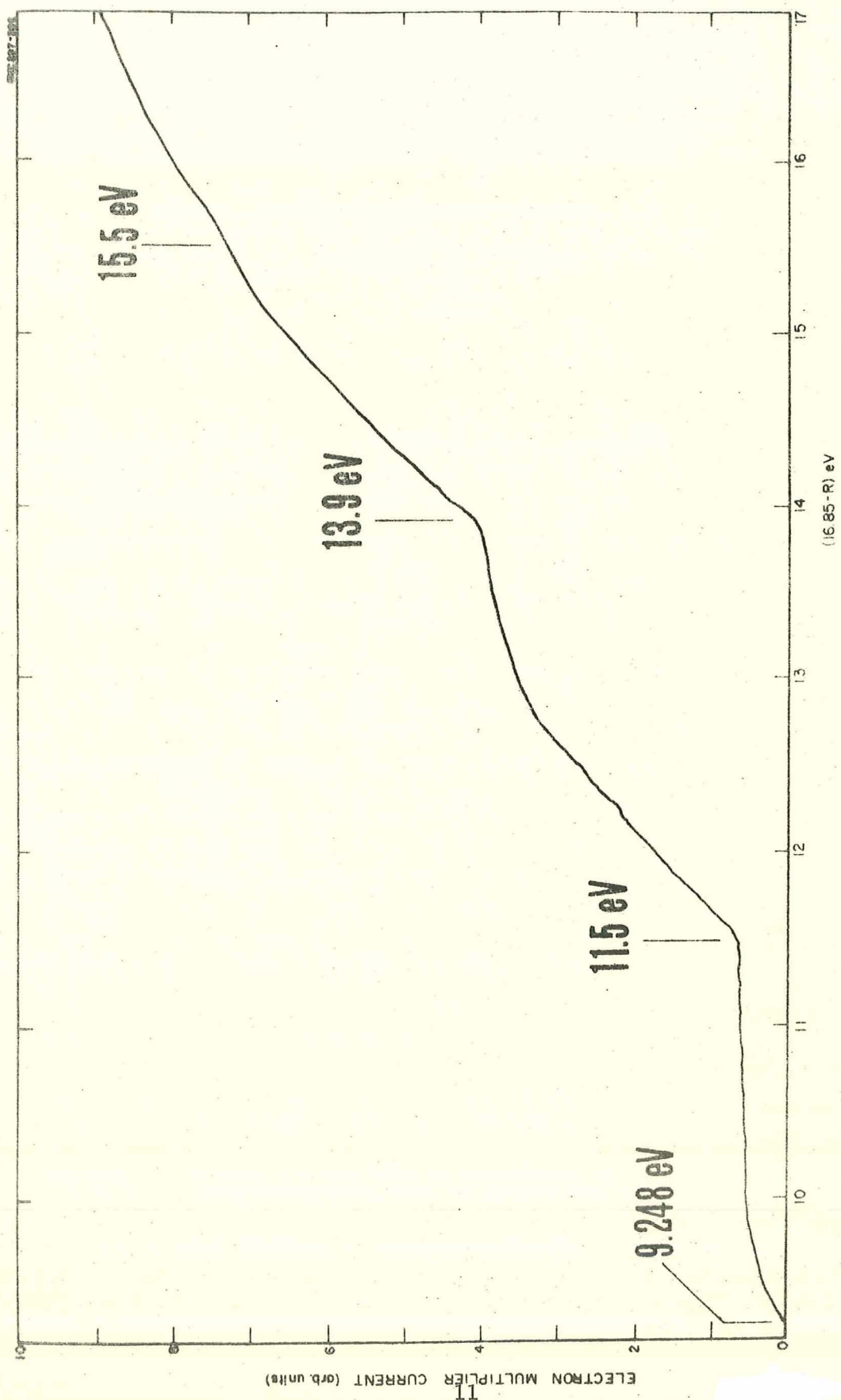


Figure 3: 735.89Å (16.85 eV) Photoelectron retarding potential curve for benzene. Neon was used in the light source.

present data and the arguments presented here that no experimental data to date have shown the existence of electronic states between 9.25 and 11.5 eV. It seems reasonable at this point to accept this fact and to reinterpret the energy assignments of the  $\pi$  and  $\sigma$  orbitals as has been done by Lindholm and colleagues. (29,30)

## 2. Photon Scattering by Argon in the VUV

Experimental determinations of photon-scattering cross sections in the vacuum ultraviolet have been limited by severe experimental difficulties. All experimental<sup>(31-34)</sup> data available for argon atoms at wavelengths shorter than  $2000\text{\AA}$  are listed in Table 1, together with some corresponding values obtained theoretically<sup>(35-37)</sup> and calculated from empirical extrapolations of measured refractive indices.<sup>(38)</sup> There are no data close to the resonance lines at 1048.218 and  $1066.660\text{\AA}$ . We have attempted such measurements using a method similar to that of Gill and Heddle<sup>(32)</sup> but with dispersed radiation. This modification, with its concomitant reduction of intensity, is necessary in regions where the scattering cross section changes rapidly with wavelength.

Radiant flux from a hydrogen source was dispersed by a one-half meter Seya monochromator with a  $\text{MgF}_2$  coated aluminized grating blazed at  $1500\text{\AA}$ . The spectral bandpass was set at  $3\text{\AA}$ . Monochromatic flux entered the scattering cell through an LiF window and the transmitted flux was monitored with an EMI 9514 S phototube coated with sodium salicylate. Flux scattered through  $90^\circ$  in the Rowland plane of the monochromator was de-

tected with an EMR 541 H-08-18 phototube which was sensitive in the region 1050 to about 1650 $\text{\AA}$ . Photon counting techniques were employed.

The experimental method was tested at 1607 $\text{\AA}$  by measuring the ratio of the scattering cross section of argon to that of helium. Since the value of the helium cross section has been calculated precisely<sup>(39)</sup> the cross section of argon could be calculated and was found to be  $9.2 \pm 0.7 \times 10^{-25} \text{ cm}^2$ . This value fits well with the available experimental data<sup>(34)</sup>

and is in good agreement with the corresponding theoretical value  $8.85 \times 10^{-25} \text{ cm}^2$ .<sup>(35)</sup> This result confirmed the applicability of the technique and the helium measurements, which for reasons of intensity were confined to this wavelength, illustrated its high sensitivity. The flux scattered from argon per unit incident flux was also measured at 1216, 1176, 1162 and 1146 $\text{\AA}$  and found to increase linearly with pressure, see Figure 4. The scattering cross sections at these wavelengths are not directly proportional to the slopes of these lines. Corrections are required for variations with wavelength of the sensitivities of the two phototubes, the transmittances of LiF windows, and possibly, the fluorescent efficiency of sodium salicylate the degree of polarization of the dispersed radiation, and the angular distribution of the scattered flux relative to

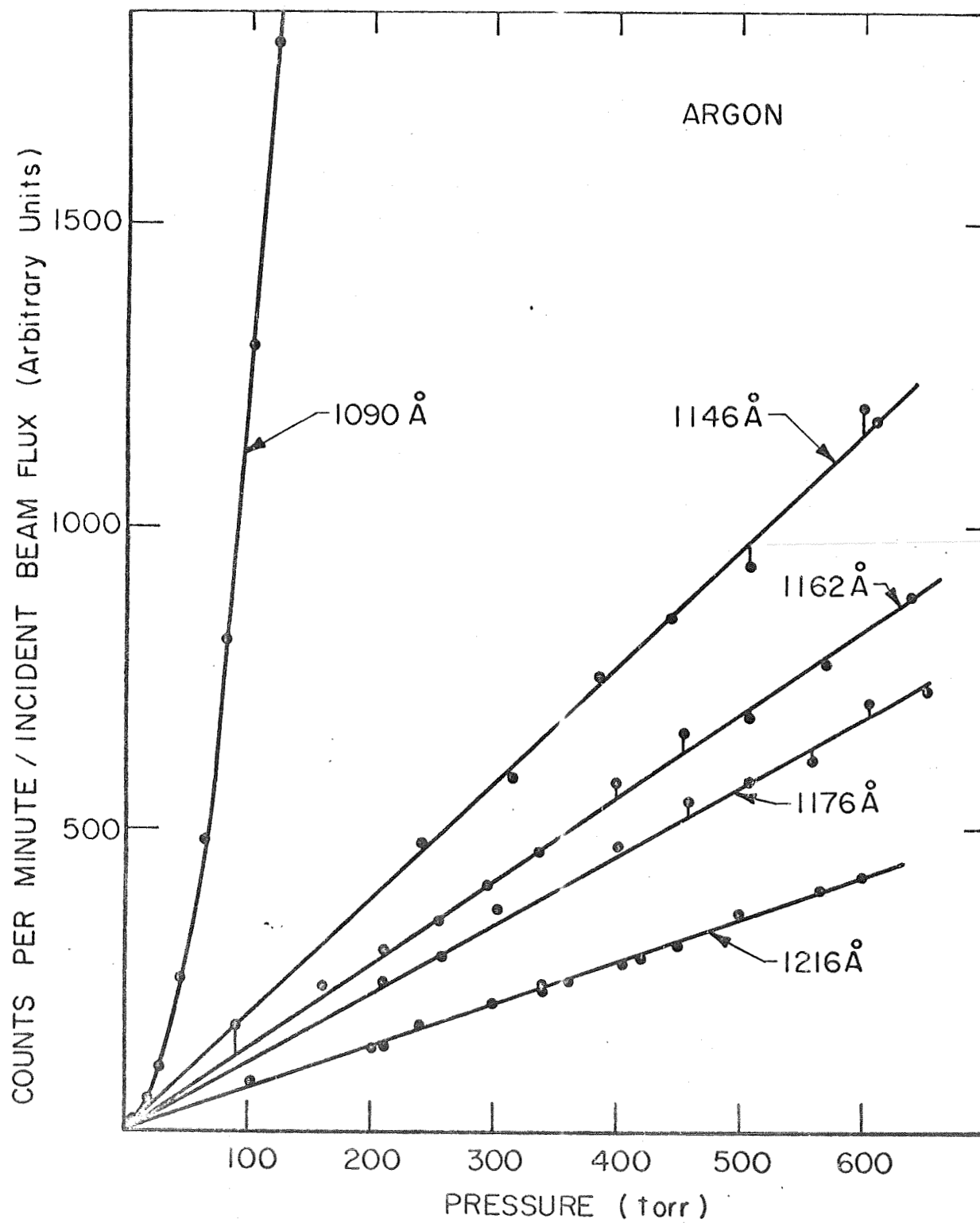


Figure 4: The scattered flux from argon as a function of pressure



the electric vector of the incident flux. Changes in these parameters could be measured but with insufficient accuracy to test the theoretical values.

At  $1090\text{\AA}$  the scattered flux was found to increase not linearly, but quadratically with pressure. This same quadratic dependence was observed in an attenuation experiment in which the factor  $1/n_1 \ln I_0/I$  was determined as a function of  $n_1$ , where  $n_1$  is the argon atom concentration and  $I_0$  and  $I$  are the incident and transmitted fluxes, respectively. The results, contained in Figures 5 and 6 are ascribed to the presence of quasi-molecules (atoms in collision or bound by Van der Waals forces) the concentration of which increases as the square of the atom concentration. The existence of such quasi-molecules has long been recognized. However, their role has not been considered in scattering experiments at wavelengths where it is probably important, for example, in the determinations of the photon scattering cross section of krypton at  $1216\text{\AA}$ .<sup>(32)</sup>

The data contained in Figures 5 and 6 can be used to estimate the magnitude of the  $\text{Ar}_2$  scattering cross section at  $1090\text{\AA}$ . The ratio of the scattered flux ( $f$ ) at  $1090\text{\AA}$  to that at  $1216\text{\AA}$  can be expressed in

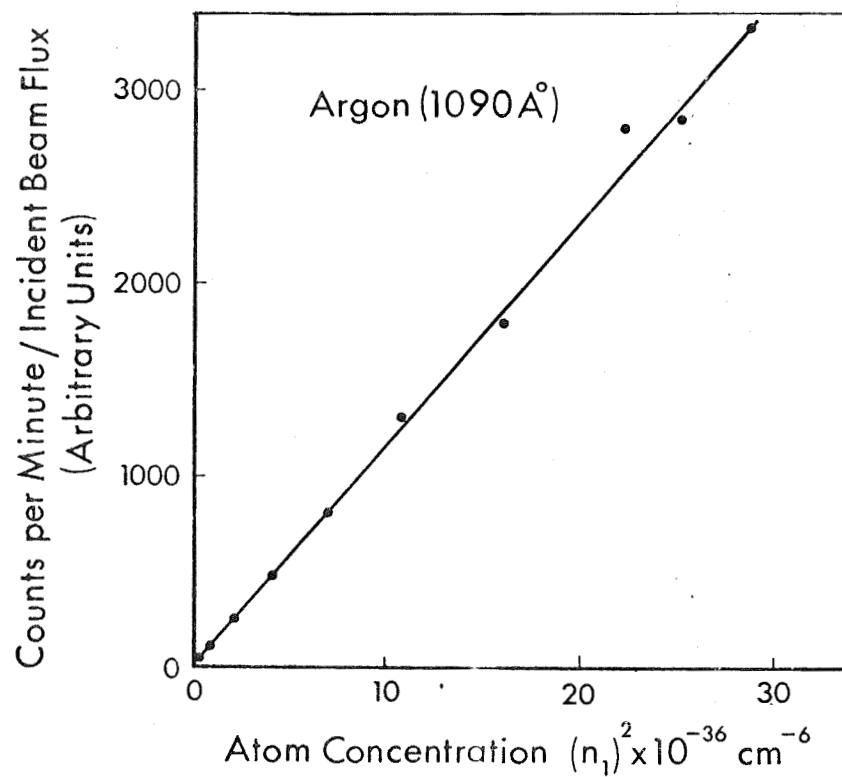


Figure 5: The scattered flux from argon as a function of the (atom concentration)<sup>2</sup>.

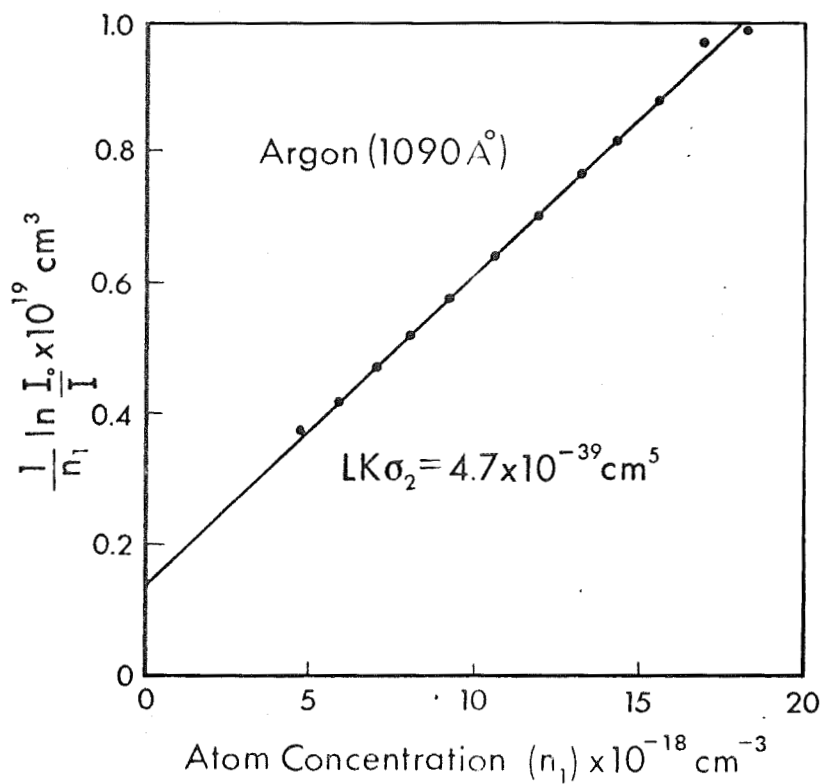


Figure 6: Attenuation of 1090Å radiation by argon. The letters  $I_0$  represent the incidents and transmitted photon flux, respectively. The length of the absorption path  $L$  was 22.4 cm.

terms of the ratio of the products of the corresponding scattering cross sections, the numbers of scatterers, and the photon fluxes incident upon the scattering volume. If we assume that at 1216Å the scattering is predominantly by argon atoms and at 1090Å by quasi-molecules, as is evidenced in Figure 44, then

$$\frac{f_{(1090)}}{f_{(1216)}} = \frac{I_0(1090) \exp \left\{ - (\sigma_{a2} + \sigma_{s2})(1090) n_2 L \right\} \sigma_{s2}(1090) n_2}{I_0(1216) \exp \left\{ - (\sigma_{s1})(1216) n_1 L \right\} (\sigma_{s1})(1216) n_1}$$

where

$n_2$  is the  $\text{Ar}_2$  concentration

$L$  is the total radiation path length in the gas

$\sigma_{a2}$  is the absorption cross section of  $\text{Ar}_2$ , and

$\sigma_{s2}$  and  $\sigma_{s1}$  are the scattering cross sections of  $\text{Ar}_2$  and  $\text{Ar}$ , respectively.

The ratio  $n_2/n_1 = Kn_1$  is known since  $K$ , the equilibrium constant for the formation of  $\text{Ar}_2$  molecules, is related to the second virial coefficient of the equation of state of argon, <sup>(40, 41)</sup> which is known to be -15.9 cc/mole. Thus the required scattering cross section is given by the following equation

$$\sigma_{s2}(1090) = \left\{ \frac{f_{(1090)}/I_0(1090)}{f_{(1216)}/I_0(1216)} \right\} \left\{ \frac{\sigma_{s1}(1216)}{Kn_1} \right\} \left\{ \frac{\exp(-\sigma_{s1}(1216)n_1 L)}{\exp(-[\sigma_{a2} + \sigma_{s2}](1090)Kn_1^2 L)} \right\}$$

The first term on the right hand side of this equation is known. The second term is also known subject to the corrections previously mentioned

and discussed quantitatively later. The value taken for  $\sigma_{s1}(1216)$  was  $56.6 \times 10^{-25} \text{ cm}^2$  this being the mean of those given in Table 1. The third term involves the undertermined quantity  $(\sigma_{a2} + \sigma_{s2})(1090)$ . This is the attenuation cross section labeled  $\sigma_2$  in Figure 6. If forward scattering is ignored the attenuation cross section can be obtained directly from the slope of the line shown in Figure 6 which is described by the equation

$$\frac{1}{n_1} \ln \left( \frac{I_0}{I} \right)_{(1090)} = L (\sigma_{s1})_{(1090)} + L (\sigma_{a2} + \sigma_{s2})_{(1090)} K n_1$$

It has the value  $8.0 \times 10^{-18} \text{ cm}^2$ . In principle, the intercept of this line on the ordinate allows the atomic scattering cross section to be determined. However, in practice this is not possible because of absorption by trace impurities such as water vapor.

The value of the  $\text{Ar}_2$  scattering cross section at  $1090\text{\AA}$  thus obtained is  $1.6 \times 10^{-18} \text{ cm}^2$ . This value has been corrected by the factors 1.39 and 0.95 which account, respectively, for a decrease in detection efficiency of the scattered flux and an increase in the polarization of the dispersed incident flux at  $1090\text{\AA}$  relative to  $1216\text{\AA}$ . The polarization was measured by the method of Rabinovitch, et al.<sup>(42)</sup> and the factor 0.95 determined according to equation 16 of reference (43).

In conclusion, we have shown that scattering cross sections can be measured by the method of Gill and Heddle<sup>(32)</sup> but with dispersed radiation. Such measurements give a sensitive test for the presence of rare-gas quasi-molecules. The second virial coefficient of argon has been used to deduce the ratio  $n_2/n_1$  which has a value of  $8.6 \times 10^{-5}$  at 100 Torr. This is in fair agreement with the observed ratio of  $10^{-4}$ .<sup>(44)</sup> The molecular

TABLE 1.

Photon Scattering Cross Sections of Ar ( $\sigma_{sl}$ )  $\times 10^{25} \text{ cm}^2$ \*

Wavelength ( $\text{\AA}$ )	Extrapolation Formula Ref. 8	E X P E R I M E N T A L					C A L C U L A T I O N			
		Ref. 31	Ref. 32	Ref. 33	Ref. 34	This paper	Ref. 35	Ref. 36	Ref. 37	
1850	4.3	4.1			4.3		4.3	4.3		
1805	4.8	4.6			4.9		4.9	4.8		
1607	8.7				8.7	9.2	8.9			
1216	57.7		62.2	64.0	52.7		49.6	58.3	51.5	
1210	60.8	66.0			55.2		51.5	61.5		
1110	271				194		102			
1090	604						385			

\*The reader is referred to the original papers for discussions of errors.

cross section at  $1090\text{\AA}$  must be large for this minority constituent to dominate the scattering. A method for estimating this cross section has been described and a value of  $1.6 \times 10^{-18} \text{ cm}^2$  obtained. Two sources of uncertainty exist. First, the angular distribution of the scattered flux relative to the electric vector of the incident flux may be different at  $1090$  and  $1216\text{\AA}$ . Second, radiation may be scattered at wavelengths longer than  $1650\text{\AA}$ , the detection limit of the EMR phototube. However, these factors do not affect the attenuation cross section ( $8.0 \times 10^{-18} \text{ cm}^2$ ) which constitutes an upper limit to the quasi-molecular scattering cross section. The existence of rare-gas quasi-molecules complicates the determination of oscillator strengths of the resonance transitions by the scattering method.

### 3. Yield of Ions resulting from Photoionization

A variety of small molecules has been studied with the photoionization mass spectrometer to determine the yield of fragment ions resulting from photoionization. Of particular interest in this work was the investigation of the wavelength dependence of product ions near their thresholds of appearance, because it allows the determination of appearance potentials, which in turn provide information on important thermodynamic properties of the ions and their parent molecules.

The techniques involved have been reported previously <sup>(45,46)</sup> and only a brief summary is required here. The photoionization mass spectrometer employed involves a 1/2 meter Seya grating monochromator with the slits set to provide a spectral resolution of about  $3.5\text{\AA}$  at half-width. The monochromator exit slit also serves as the entrance slit to the ion source chamber. After passing the ion chamber, the radiation is registered on a sodium-salicylate-coated photomultiplier. From the ion chamber, ions are withdrawn at right angles to the light beam through an aperture of 3 mm diameter. A concave repeller provides a concentric field configuration which enhances the collection of ions. Subsequently, the ions are focused onto the entrance aperture of a 180 degree magnetic analyzer, behind the exit orifice of which the ions are registered by means of an electron multiplier detector. An electrometer readout circuit and recording equipment complete the experimental arrangement.

The experimental procedure entailed taking simultaneous recordings as a function of wavelength of the photomultiplier current and the ion current. For this purpose, the magnet current of the mass spectrometer was adjusted to allow the desired ionic species to pass the mass analyzer, and the wavelength drive of the monochromator was actuated. Two types of



light sources were used which gave overlapping spectra in the wavelength region of interest: (a) a dc cold cathode type source operated with hydrogen as the filler gas provided a usefully intense spectrum between 900 and 1300 $\text{\AA}$ ; (b) a Weissler type repetitive spark source operated with argon gave a usefully intense spectrum between 450 and 1000 $\text{\AA}$ . Both light sources emit line spectra, but the population of emission lines made available is sufficiently dense to provide data points not more than 10 $\text{\AA}$  apart over most of the investigated wavelength range. The ion yield curves thus obtained are sufficiently well defined to allow their extrapolation to threshold. Since, in addition, polyatomic molecules do not usually exhibit narrow structure in absorption and photoionization cross sections, the many line radiation source employed here suffice for this study.

To date, detailed data have been obtained for methane, methanol, formaldehyde and formic acid. These substances were introduced to the ion source chamber via an appropriate leak valve at a pressure of about  $10^{-3}$  Torr. At these high source pressures satellite mass peaks due to secondary ion reactions were observed but their intensity was insignificant. These secondary peaks, for example M33 from methanol, could be identified easily from the fact that their thresholds coincided with that of the parent peaks. Although the effect of the satellite ion peaks could be reduced by working at lower pressures, it was advantageous to make use of the generally good ion intensities provided in the  $1 \times 10^{-3}$  Torr pressure regime and to tolerate the appearance of secondary ions.

Figure 7 shows, as an example, the ion yields for  $\text{CH}_4^+$  and  $\text{CH}_3^+$  observed in the photoionization of methane in the 800-1000Å wavelength region. From the yield curves the onsets can be determined by extrapolation. We find the thresholds for  $\text{CH}_4^+$  at 976Å and for  $\text{CH}_3^+$  at 874Å. After correction for the involved spectral resolution, the resulting threshold wavelengths and associated energies are

$\text{CH}_4^+$	$973 \pm 3\text{Å}$	$12.74 \pm 0.04 \text{ eV}$
$\text{CH}_3^+$	$871 \pm 3\text{Å}$	$14.23 \pm 0.06 \text{ eV}$

These values are in good agreement with those determined by Dibeler, et al<sup>(47)</sup> and by Chupka.<sup>(48)</sup>

In a similar manner, thresholds for various ions have been determined for methanol and formaldehyde. These are given in Table 2. The relative ion yields as a function of wavelength for these compounds and for formic acid have not yet been evaluated in detail, but as supplementary information we give in Table 3 the ion distribution for all the compounds investigated at the photoionizing wavelength of 801Å.

The threshold energies assembled in Table 2 will now be used to derive some important selected thermodynamic properties. From the appearance potentials of the parent ions of methanol and formaldehyde one obtains the ionization energies 10.85 eV for  $\text{CH}_3\text{OH}$  and 10.89 eV for  $\text{CH}_2\text{O}$ . These values are in excellent agreement with those determined by Watanabe<sup>(49)</sup> and collaborators using a different photoionization method. Next consider the appearance potentials for  $\text{CH}_3^+$  and  $\text{CH}_2^+$  from methanol. After subtraction

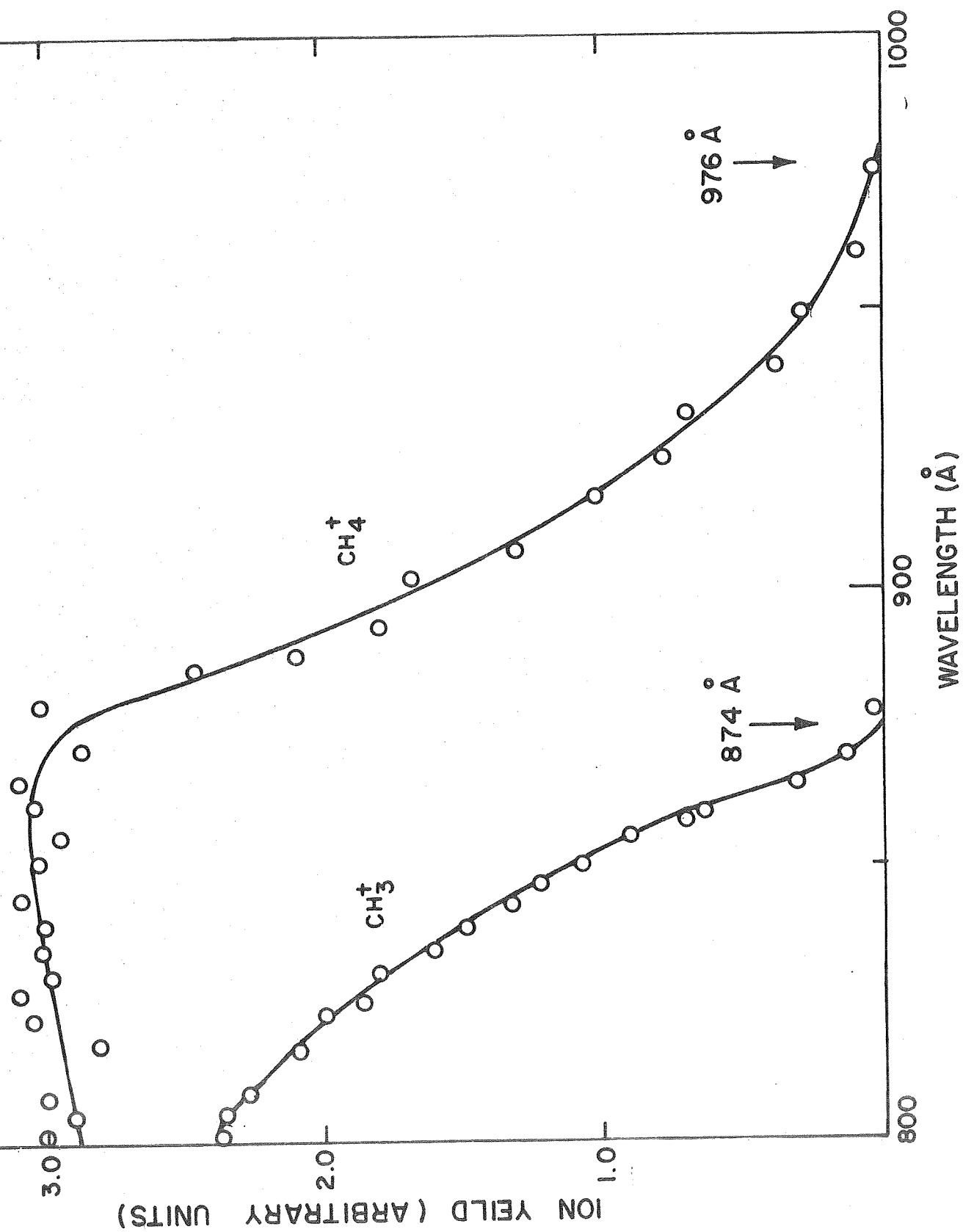


Figure 7

TABLE 2

Photoionization Thresholds for the Appearance of Ions in Methanol and in  
Formaldehyde

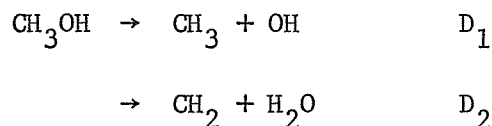
Compound	Ion	Threshold Wavelength ( $\text{\AA}$ )		Energy (eV)
		Observed	Corrected	
$\text{CH}_3\text{OH}$	M32	$1145 \pm 3$	$1142 \pm 3$	$10.85 \pm 0.03$
	M31	$1077 \pm 3$	$1074 \pm 3$	$11.54 \pm 0.03$
	M30	$1033 \pm 10$	$1030 \pm 10$	$12.04 \pm 0.12$
	M29	$952 \pm 7$	$949 \pm 7$	$13.06 \pm 0.10$
	M15	$900 \pm 3$	$897 \pm 3$	$13.82 \pm 0.04$
	M14	$883 \pm 5$	$880 \pm 5$	$14.09 \pm 0.08$
$\text{CH}_2\text{O}$	M30	$1142 \pm 2$	$1139 \pm 2$	$10.89 \pm 0.02$
	M29	$1046 \pm 3$	$1043 \pm 3$	$11.89 \pm 0.03$
	M 2	$807 \pm 3$	$804 \pm 3$	$15.42 \pm 0.06$
	M 1	$715 \pm 3$	$712 \pm 3$	$17.41 \pm 0.07$

TABLE 3

ION YIELDS FOR METHANE, METHANOL, FORMALDEHYDE & FORMIC ACID AT 801Å

<u>Substance</u>	<u>m/e</u>	<u>Relative Ion Yield</u>
Methane	16	0.585
	15	0.414
Methanol	32	0.443
	31	0.492
	30	0.009
	29	0.028
	15	0.031
Formaldehyde	30	0.433
	29	0.550
	28	0.016
Formic Acid	46	0.462
	45	0.286
	41	0.003
	32	0.028
	31	0.055
	30	0.003
	29	0.100
	18	0.064

of the spectroscopic ionization potentials<sup>(50)</sup> for  $\text{CH}_3$  and  $\text{CH}_2$ ,  $I(\text{CH}_3) = 9.843 \text{ eV}$  and  $I(\text{CH}_2) = 10.396 \text{ eV}$ , respectively, one obtains the dissociation energies for the processes



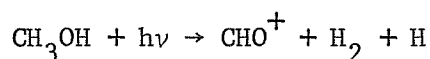
The values thus derived:  $D_1 = 3.98 \pm 0.04$  and  $D_2 = 3.69 \pm 0.08$  can be utilized to derive the heats of formation of the  $\text{CH}_3$  and  $\text{CH}_2$  radicals by virtue of the relations:

$$\begin{aligned}D_1 &= \Delta H_f(\text{CH}_3) + \Delta H_f(\text{OH}) - \Delta H_f(\text{CH}_3\text{OH}) \\ D_2 &= \Delta H_f(\text{CH}_2) + \Delta H_f(\text{H}_2\text{O}) - \Delta H_f(\text{CH}_3\text{OH})\end{aligned}$$

The resulting heats of formation are  $\Delta H_f(\text{CH}_3) = 1.49 \pm 0.04 \text{ eV} = 34.3 \pm 1 \text{ kcal/mole}$ , and  $\Delta H_f(\text{CH}_2) = 4.07 \pm 0.08 = 93.6 \pm 2 \text{ kcal/mole}$ . These values are in good agreement with those derived by Chupka<sup>(48)</sup> and by Dibeler, et al<sup>(47)</sup> from the photoionization of methane and  $\text{CH}_3$  radicals, although Chupka's values are more precise. From the threshold of  $\text{CHO}^+$  appearance from  $\text{CH}_3\text{OH}$ , the heat of formation of  $\text{CHO}^+$  can be derived via the relation

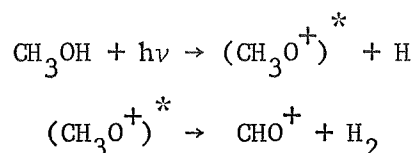
$$A(\text{CHO}^+) = \Delta H_f(\text{H}) + \Delta H_f(\text{CHO}^+) - \Delta H_f(\text{CH}_3\text{OH})$$

which assumes that the process responsible for the formation of  $\text{CHO}^+$  is

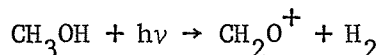


Since the threshold of  $\text{CHO}^+$  occurs at a higher energy than that of  $\text{CH}_2\text{O}^+$  of  $\text{CH}_3\text{O}^+$  it is reasonable to assume that the above reaction requires two

steps, with one of these ions as an intermediate. For example,

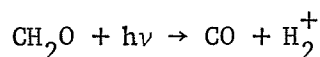


Here, the asterisk indicates that the intermediate ion must be internally excited to dissociate further in the process of  $\text{CHO}^+$  formation. Since the dissociation process may require an activation energy, the threshold of  $\text{CHO}^+$  formation can provide only an upper limit to the heat of formation of  $\text{CHO}^+$ . The present data yield  $\Delta H_f (\text{CHO}^+) \leq 8.62 \pm 0.10 \text{ eV} = 198 \pm 2 \text{ kcal}$ . This value is in excellent agreement with the heat of  $\text{CHO}^+$  formation previously derived by us from the photoionization of formaldehyde (see below), formic acid, and acetaldehyde. <sup>(51)</sup> It thus appears that the activation energy involved in the dissociation of the intermediate is negligible. From the threshold of  $\text{CH}_2\text{O}^+$  formation we find that the energy involved is by 0.19 eV or 4.4 kcal higher than predicted on account of the process

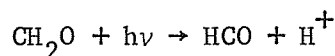


for which all the required thermodynamic values are known. Thus it appears that the intermediate for  $\text{CHO}^+$  formation is  $\text{CH}_3\text{O}^+$  rather than  $\text{CH}_2\text{O}^+$ . On the other hand, the heat of formation for  $\text{CH}_3\text{O}^+$  derived from the threshold of its observation is  $\Delta H_f (\text{CH}_3\text{O}^+) = 7.20 \pm 0.03 \text{ eV} = 166 \pm 1 \text{ kcal}$ , in good agreement with a value recently derived by Haney and Franklin <sup>(52)</sup> from electron impact mass spectrometry with consideration of the excess kinetic energy of the fragments.

Similar considerations apply to the data for formaldehyde. From the threshold of  $\text{CHO}^+$  formation one obtains  $\Delta H_f (\text{CHO}^+) = 8.51 \pm 0.03 \text{ eV} = 196 \pm 1 \text{ kcal}$ . This result has been reported previously.<sup>(51)</sup> The formation of  $\text{H}_2^+$  is due to the process



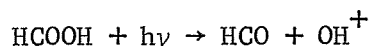
The threshold of 15.42 eV is in good agreement with that calculated for this process from known available thermochemical values  $A (\text{H}_2^+) = 15.40 \text{ eV}$ . The formation of  $\text{H}^+$  is associated with



This process allows the derivation of the heat of formation of CHO. Subtracting from the threshold energy for  $\text{H}^+$  formation the ionization potential of the hydrogen atom,  $I (\text{H}) = 13.595 \text{ eV}$ , gives the bond dissociation energy for formaldehyde  $D (\text{CHO} - \text{H}) = 3.82 \text{ eV} = 88 \pm 2 \text{ kcal/mole}$ . The corresponding value for the heat of formation of CHO is  $\Delta H_f (\text{HCO}) = 0.43 \pm 0.07 \text{ eV} \approx 10 \text{ kcal/mole}$ . From this value, the dissociation energy of the HCO radical can be calculated as  $D (\text{H} - \text{CO}) = 15.7 \text{ kcal}$ . In deriving these values the new heat of formation of formaldehyde,<sup>(53)</sup>  $\Delta H_f (\text{CH}_2\text{O}) = -25.9 \text{ kcal/mole}$ , has been used. The value for  $D (\text{CHO} - \text{H})$  derived here is the high value of the two possibilities discussed in the literature. Similarly, the value for  $D (\text{H} - \text{CO})$  derived here is the low value for the discussed two possibilities. Independent evidence for  $D (\text{CHO} - \text{H}) = 88 \text{ kcal/mole}$  has been derived previously by Haney and Franklin.<sup>(52)</sup> From a detailed discussion of previous data, Kerr<sup>(54)</sup> has also favored this value.



Although an analysis of the formic acid data is even less complete than the ones discussed above, a check has been made on the heat of formation of the CHO radical by the observation of the threshold for the process



which was observed to occur at  $690\text{\AA}$ , corresponding to 17.97 eV. The value for the heat of formation of HCO derived from this process is  $\Delta H_f(\text{CHO}) = 0.45 \text{ eV} = 10.5 \text{ kcal}$ . This is in good agreement with the value found above from formaldehyde, supporting the high value for  $\Delta H_f(\text{CHO})$  and for  $D(\text{CHO} - \text{H})$ .

#### 4. Measurement of Ionic Mobilities

The effort under this heading represents a continuation of previous work concerning the title subject. It has been demonstrated previously<sup>(55)</sup> that the photoionization mass spectrometer technique can be employed to obtain reliable drift velocity data for mass analyzed ions produced by photoionization. In this manner it is possible, in principle, to pre-select the energy state of the ion by an appropriate choice of varying wavelengths, and to identify the ion subjected to measurement by the employed mass spectrometer.

The experimental set up and the applied experimental procedures have been described in detail previously<sup>(55,56)</sup> and will be summarized only briefly here. The cylindrical ion chamber configuration employed for this application of the instrument is conventional in that ions formed along the axis of this light beam are driven to the ion exit aperture

by an electric field established perpendicular to the direction of the light beam. The plane repeller is supported by a hollow stem so that the gas pressure in the source can be measured directly with an attached McLeod manometer. As a consequence of the ion source geometry the electric field is inhomogeneous everywhere except in the vicinity of the axis of ion removal. The field in this region was calculated from the applied voltage and from the distance between the repeller and the ion exit aperture, the positions of which were adjusted to a spacing of 0.70 cm. A small correction was required to take into account the slight field inhomogeneity near the repeller. This was shown by a field plotting method previously. (55)

The light source is a Weissler type repetitive spark source, providing 120 pulses per minute of about one microsecond duration each. This time is sufficiently short to provide an essentially instantaneous ion deposition, unless the residence time of the ions in the ion chamber becomes comparable. Under the applied conditions of pressure and electric field, ion residence times are usually longer than 10 microseconds. A further necessary experimental condition for mobility studies is that the mean free path of the ions is short compared with the drift distance. This condition is met at pressures above about 80 microns.

Due to diffusion, the ion transient broadens while drifting from the plane of origin toward the ion exit plane. Thus, the initially rectangular ion transient profile is changed to a Gaussian profile. The average ion residence time,  $\tau_0$  is defined as the time span required for the center of the profile to reach the exit aperture after deposition of the ions by the light pulse. Accordingly, the ion drift velocity is  $v = d/\tau_0$ , with  $d$  being the drift distance (0.3 cm in the present arrangement). Due to the process of diffusion broadening, some ions arrive at the exit at an earlier time  $\tau < \tau_0$ . It has been shown previously that  $\tau$  and  $\tau_0$  are related by the equation

$$\tau/\tau_0 = 1 - (f/d) (2 D\tau)^{1/2}$$

where  $D$  is the ionic diffusion coefficient and  $f$  is a factor depending upon the threshold sensitivity for the detection of the onset of the ion pulse. If the detection limit is 10 percent of the total integrated ion pulse,  $f = 1.28$ , if it is five percent of the integrated ion pulse,  $f = 1.65$ . The former factor has been used previously, <sup>(56)</sup> but due to the increased sensitivity, the latter value will be used here. Then, the measurement of both  $\tau$  and  $\tau_0$  will provide the ionic diffusion coefficient

$$D = \frac{1}{2} \frac{d^2}{f^2} \frac{(1 - \tau/\tau_0)^2}{\tau} = 1.65 \times 10^{-2} \frac{(1 - \tau/\tau_0)^2}{\tau}$$

Knowledge of the diffusion coefficient and the ionic mobility  $\mu = v/E$  provides the average energy content of the drifting ions. To derive the random energy of the ions, expressed as the ionic temperature  $T_i$ , we make use of a relation due to Einstein (see for example Huxley and Crompton) (57)

$$T = F \frac{e}{k} \frac{D}{\mu}$$

where  $e$  is the ionic charge,  $k$  is the Boltzmann constant, and  $F$  is a factor depending on the velocity distribution function of the ions. For a Maxwellian distribution  $F = 1$ , for other distributions  $F$  is usually somewhat smaller than unity. Here it will be assumed that  $F = 1$ . Then the ion temperature is defined as

$$\begin{aligned} T_i &= \frac{e}{k} \frac{1}{2} \frac{d}{f^2} \frac{(1 - \tau/\tau_o)^2}{\tau/\tau_o} E \\ &= 6.38 \times 10^2 \frac{(1 - \tau/\tau_o)^2}{\tau/\tau_o} E \end{aligned}$$

The formula then reduces the ion drift velocity, the ionic diffusion coefficient, and the ion temperature to the residence times  $\tau$  and  $\tau_o$  in the ion chamber. These quantities are determined experimentally from

the time delay of the ion pulse arriving at the mass spectrometer detector, after a group of ions is formed by the light pulse. Delay times are measured as a function of the repeller potential and a graphical extrapolation toward infinite repeller potential is applied to enable a separation of the ion source residence times from the mass spectrometer flight time of the ions. The details of this procedure have been published. (56)

Below we report data on the parent ions in three gases: argon nitrogen and oxygen.

(a) Argon

The drift velocities observed for  $A^+$  in argon are plotted in Figure 8 as a function of the reduced field strength  $E/P_0$ , for three values of the electric field and various settings of pressure in the range 70-210 microns. The lower group of data points represents measurements with the monochromator set to transmit a wavelength of  $786\text{\AA}$  (with  $3.5\text{\AA}$  halfwidth), so that only argon ions in the  $^2P_{3/2}$  ground state are formed. The upper group of data points was obtained at  $767\text{\AA}$ . In this case excited  $^2P_{1/2}$  argon ions are formed in addition to those in the ground state. At  $786\text{\AA}$ , the ion transient observed with the oscilloscope was fairly symmetric and the center of the pulse was used to derive the drift velocities. At  $767\text{\AA}$  an additional component was present, the ion transient had an asymmetric appearance, and the peak of the pulse (which was used to derive the drift velocity) shifted forward. The two types of oscilloscope traces are shown in Figure 9 for comparison. Clearly, the excited argon

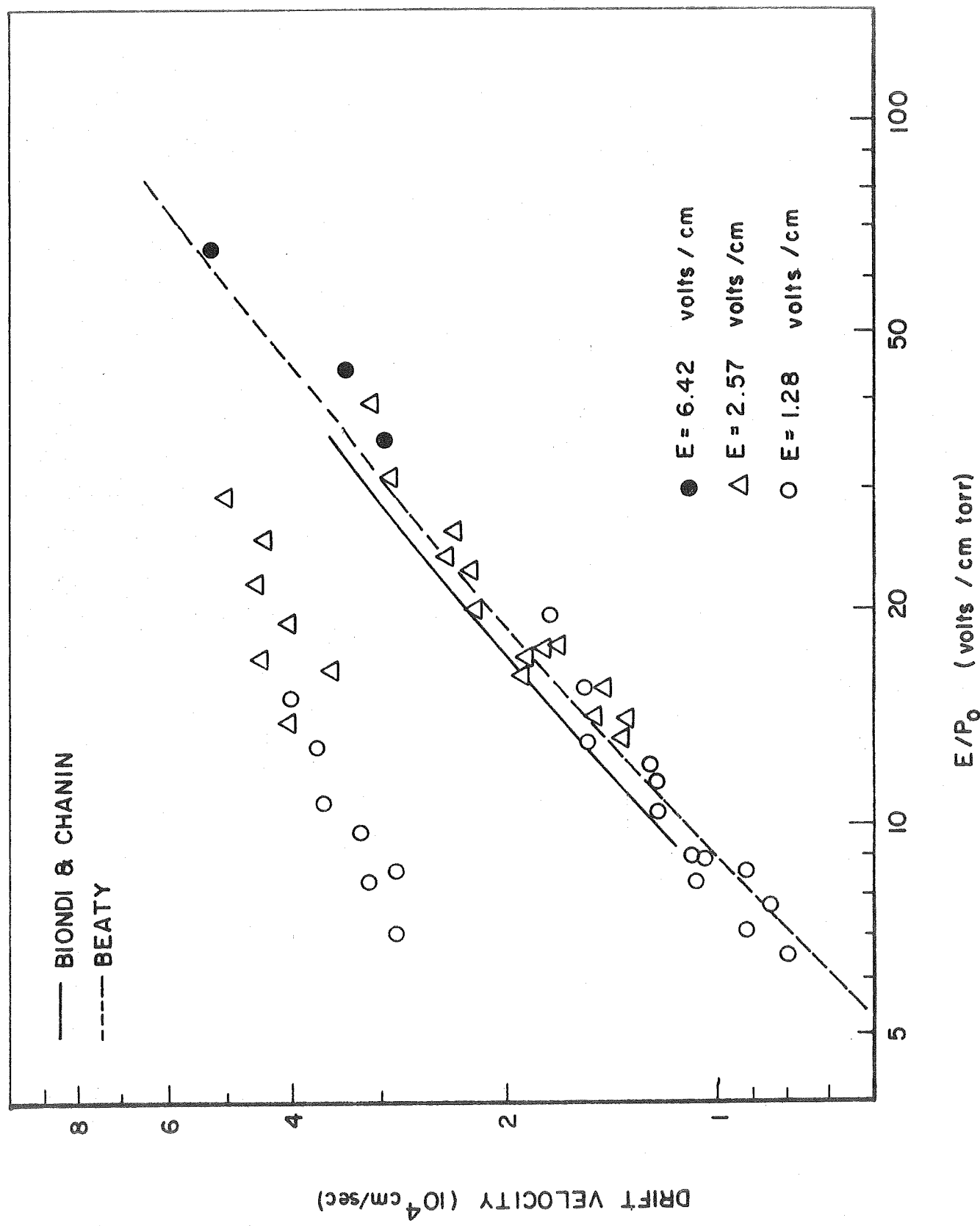


Figure 8: Drift velocities of argon ions in their parent gas. Ionizing wavelength: Lower group of points 786Å; Upper group 767Å.

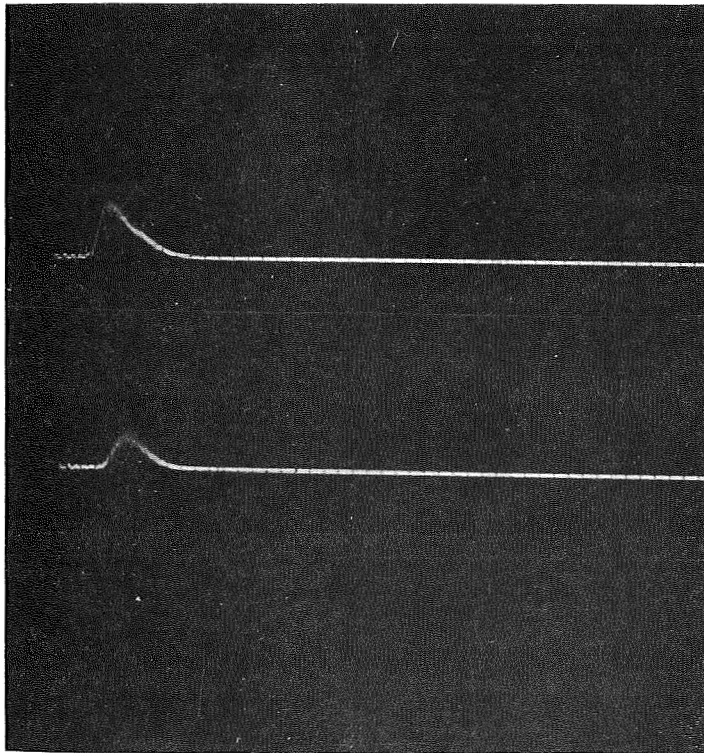


Figure 9. Argon ion transients. Lower trace:  $786\text{\AA}$ ; upper trace:  $767\text{\AA}$ .

ion moves faster than the ground state ion. Since the mobility of an ion, like its diffusion coefficient, is inversely proportional to its cross section for momentum transfer to the neutral gas, suitably averaged over the range of velocities, the data indicate that the momentum transfer cross section for the excited argon ion is smaller than that for the ground state argon ion. For both types of argon ions moving in the parent gas, the momentum transfer cross section is governed mainly by charge transfer. Theoretically one would predict, on the assumption that the reduced matrix elements governing the two charge transfer cross sections are nearly equivalent, that the difference in cross sections is due to the differences in the degeneracy of the two processes. Thus, the summation over all possible magnetic quantum number combinations indicates  $Q_{\text{ground}}/Q_{\text{excited}} = 2$ , because the resonant process  $A^+ (^2P_{3/2}) + A (^1S_0)$  is a 4 fold degenerate, while the process  $A^+ (^2P_{1/2}) + A (^1S_0)$  is 2 fold degenerate. The observed increase in mobility when going from the ground state to the excited state is about three at the lower end of the reduced field strengths. Towards higher fields, the ratio becomes smaller due to the fact that the drift velocity for the excited argon ions increases with  $E/P$  approximately with  $1/2$  power, whereas the drift velocity of ground state argon ions increases essentially linearly with  $E/P$ .

The data obtained for ground state argon ions are found to be in excellent agreement with previous measurement. Two sets of previous data are shown in Figure 8, those by Biondi and Chanin<sup>(58)</sup> are



represented by the solid line and those by Beaty, et al.<sup>(59)</sup> are indicated by the dashed line. Two more recent measurements, like the present one with mass identification, were made by McAfee, et al.<sup>(60)</sup> and by Madson and Oskam.<sup>(61)</sup> They are in good agreement with the former and the present measurements. An extrapolation of the present data to zero electric field leads to a reduced zero field mobility of  $A^+$  of  $\mu = 1.5 \text{ cm}^2/\text{sec volt}$ . It must be realized that the drift velocities of the excited argon ions cannot be measured with the same reliance as that of the ground state ions, because the two ion transients cannot be sufficiently separated so that the arrival time of the center of the excited ion transient is falsified by the contribution due to the normal argon ions. Accordingly, the data presented here for that ion species must be considered tentative. Qualitatively, however, there can be no doubt about the increased drift velocity of the excited ion compared with the ground state ion. The importance of this finding should not be underrated. It has been made possible solely by the energy differentiation provided by the method of photoionization.

The good results obtained for ground state ions in argon have encouraged measurement of diffusion coefficients and ion temperatures according to the methods outlined above. These are shown in Figures 10 and 11. The straight line in Figure 10 is calculated from the thermal, zero field mobility of the argon ions. The data points agree with the calculated diffusion coefficients, indicating that the energy that the argon ions acquire from the field is quickly passed on to the neutral argon

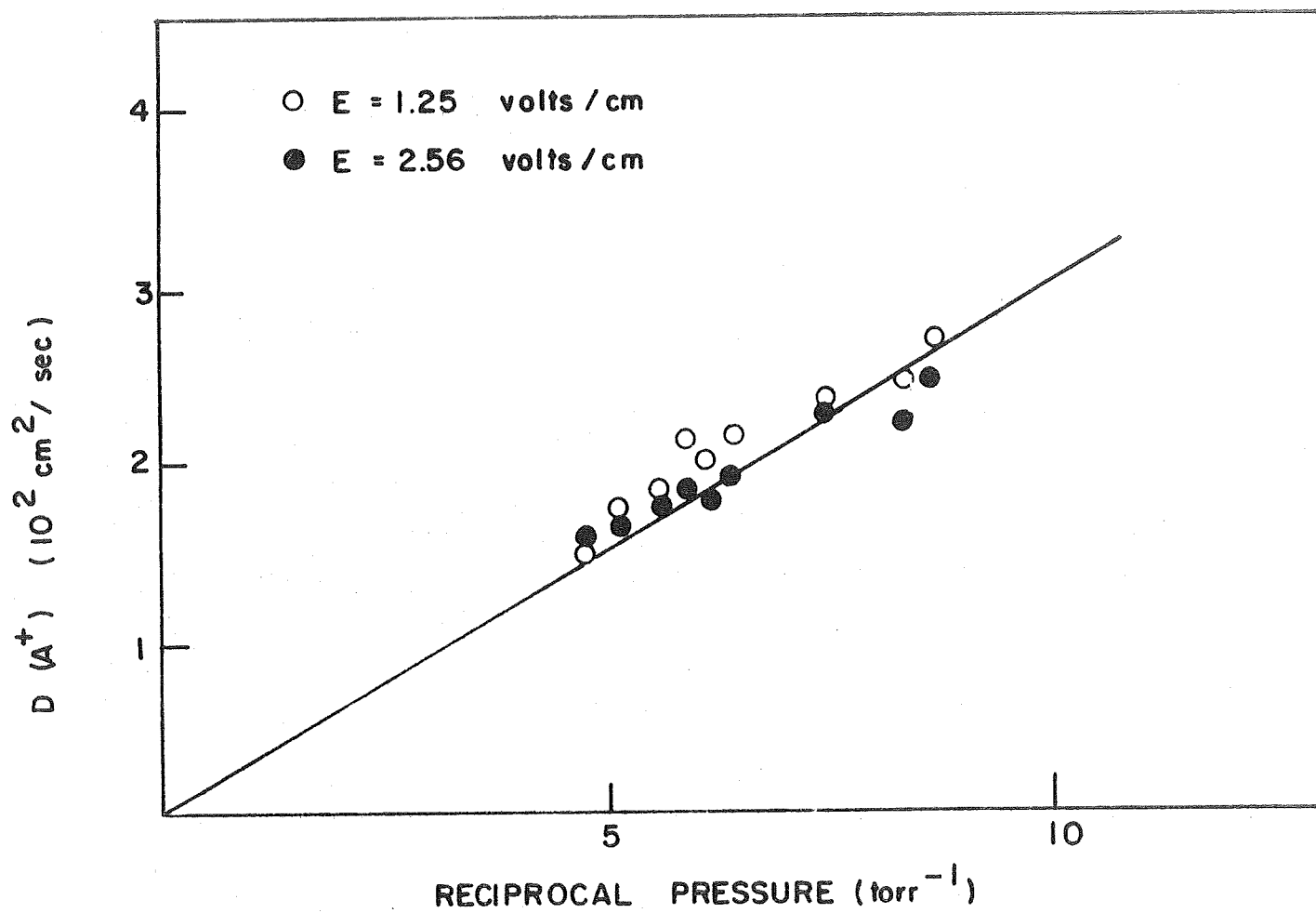


Figure 10: Diffusion coefficients for  $A^+(^2P_{3/2})$  ions in argon. Solid line calculated for thermal ions.

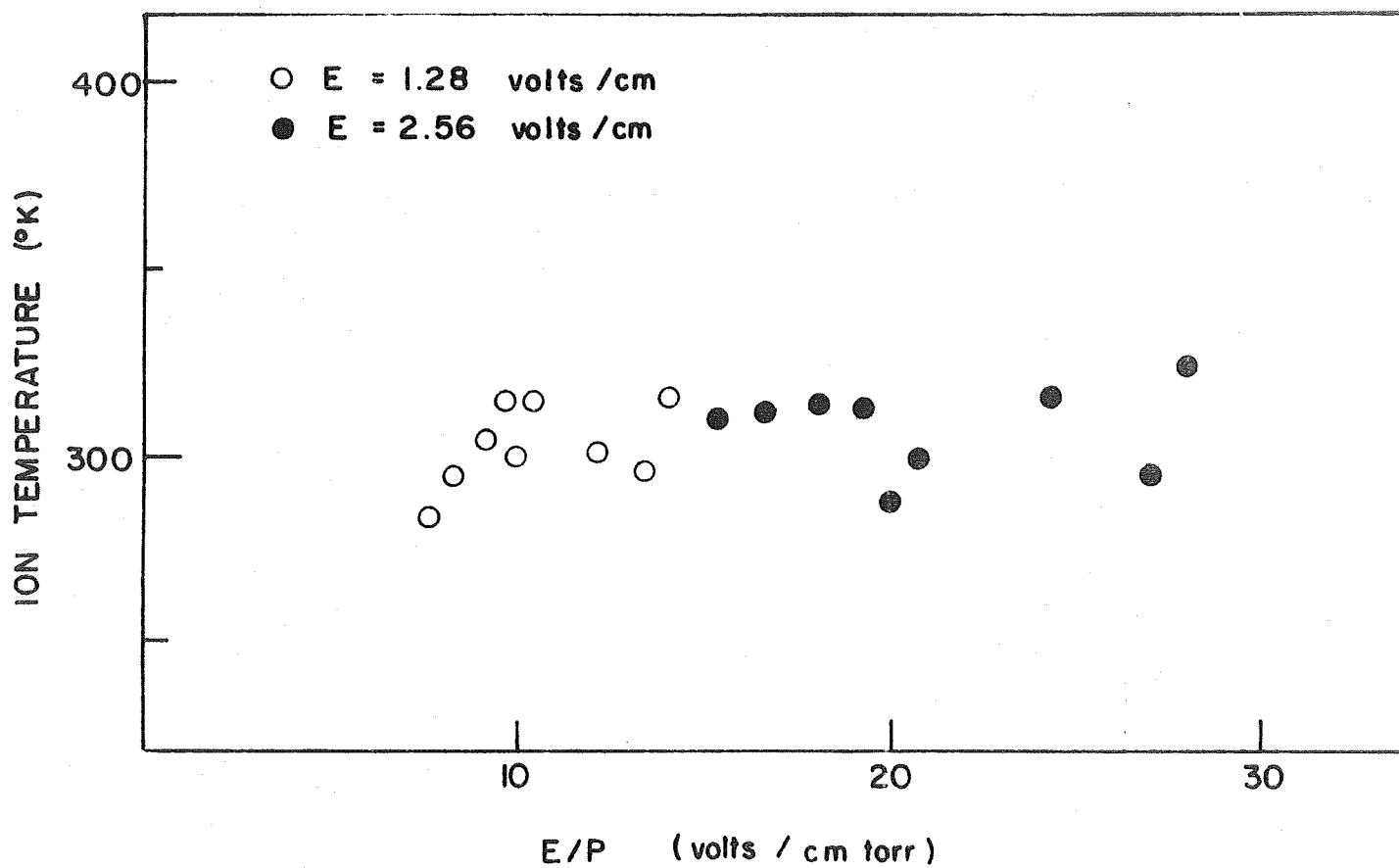


Figure 11: Temperature of  $A^{+}(^2P_{3/2})$  ions as a function of E/P.

matrix. This behavior is reflected also in the derived ion temperature, which lies only little above that corresponding to thermal ions. A considerable scatter of the data points in Figure 11 makes apparent that an accurate determination of ion temperatures is not possible by this method. However, the good agreement of ion temperature and diffusion coefficients with the expected ion behavior indicates the validity of the concepts underlying their derivation.

#### (b) Nitrogen

Drift velocities observed for nitrogen ions formed from molecular nitrogen at an ionizing wavelength of  $790\text{\AA}$  were reported previously by us and are shown in Figure 12. There is good agreement with the results of Saparoshenko<sup>(62)</sup> and Keller, et al.<sup>(63)</sup> who also used mass identification of the ions. Similar to the behavior of argon ions, an increase of drift velocities was observed for  $\text{N}_2^+$  as the ionizing wavelength was lowered. However, the mobility increase occurred at isolated wavelengths, and was then clearly recognizable as an asymmetry of the ion transient. A very strong asymmetry occurred at  $764\text{\AA}$ , and drift velocities corresponding to the peak of the ion pulse at this wavelength are shown in Figure 12 as the upper group of data points. The increase in ion mobility appears to occur at wavelengths where the emission lines available from the light source coincide with autoionization features in the  $\text{N}_2$  absorption spectrum. At  $764\text{\AA}$ , the wavelength investigated here, the line group emitted from the source overlaps the  $v(1-0)$  transition at  $764.35\text{\AA}$  of the Ogawa and Tanaka<sup>(64)</sup> progression (1) series which, having a high

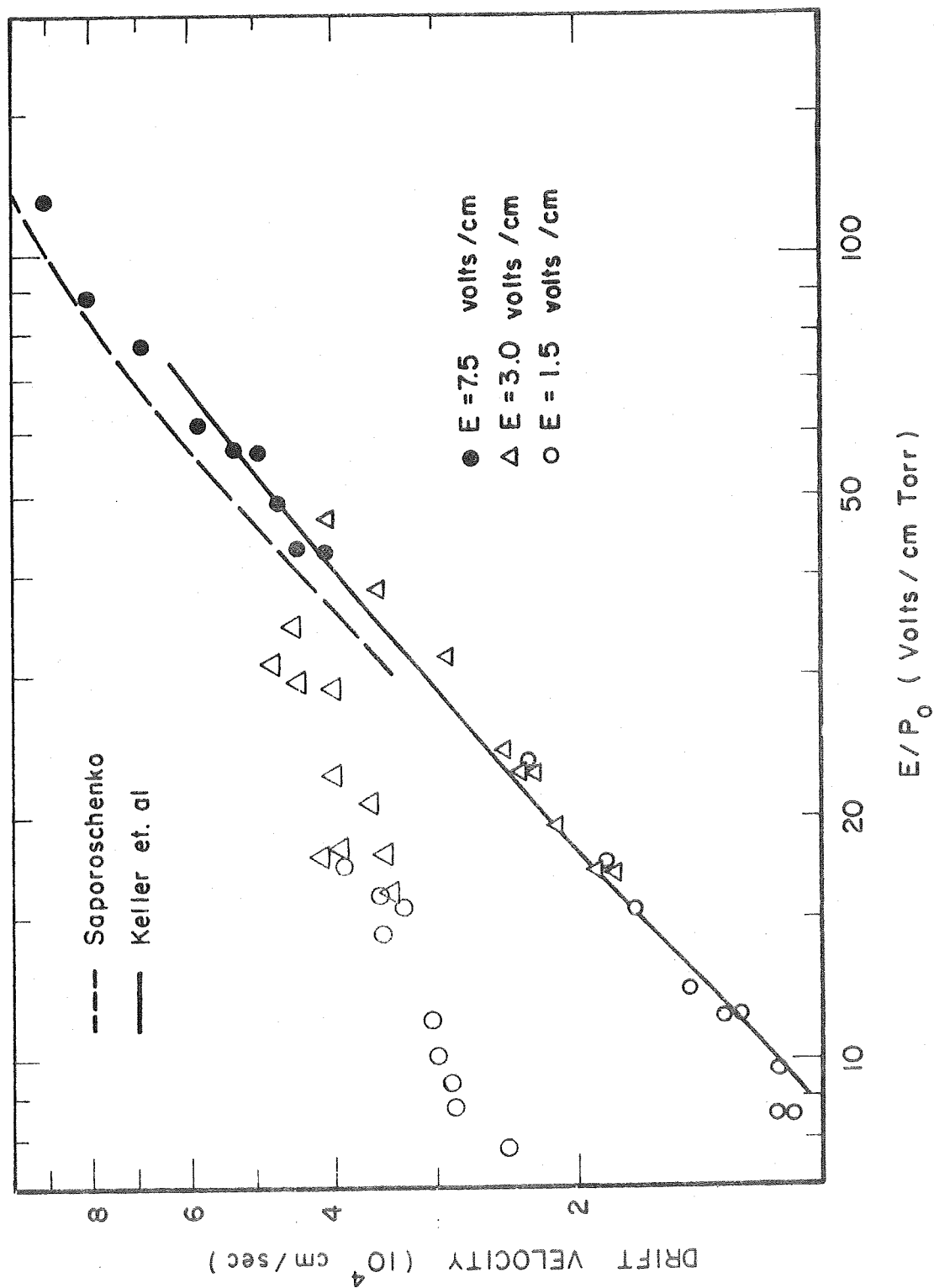


Figure 12: Drift velocities of  $N_2^+$  in nitrogen versus relative field strength. Ionizing wavelength: lower group of points 790Å; upper group of points 764Å.

ionization efficiency produces a considerable population of vibrationally excited  $N_2^+$  ( $v = 1$ ) ions. Accordingly, the increased mobility  $v$  at  $764\text{\AA}$  is due to vibrationally excited  $N_2^+$  ions, whereas at  $790\text{\AA}$  only ground state nitrogen ions are formed. Similar to the results discussed above for argon ions, the  $N_2^+$  ion mobility increases by a factor of about 3 for vibrationally excited ions. A similar behavior with  $E/P$  is observed as for ions in argon.

Figures 13 and 14 show the diffusion coefficients and the ion temperatures determined for  $N_2^+$  ( $v = 0$ ), respectively. Unlike the behavior of argon ions, the diffusion coefficients are much higher than that for thermal ions (indicated by the solid line), and the ion temperatures derived lie also considerably above thermal values. Both factors indicate an appreciable energy content of  $N_2^+$  ions in the presence of electric fields. Note also that both diffusion coefficients and ion temperatures increase as the field strength is increased.

### (c) Oxygen

The drift velocities determined for  $O_2^+$  ions as a function of  $E/P$  are shown in Figure 15. These data were obtained with an ionizing wavelength of  $1007\text{\AA}$ , and good agreement is observed with the results of previous investigations<sup>(65,66)</sup> in which the identity of the ion was inferred rather than determined. At  $1007\text{\AA}$ , photoionization of  $O_2$  may lead to  $O_2^+$  in the first vibrationally excited state, but from the results

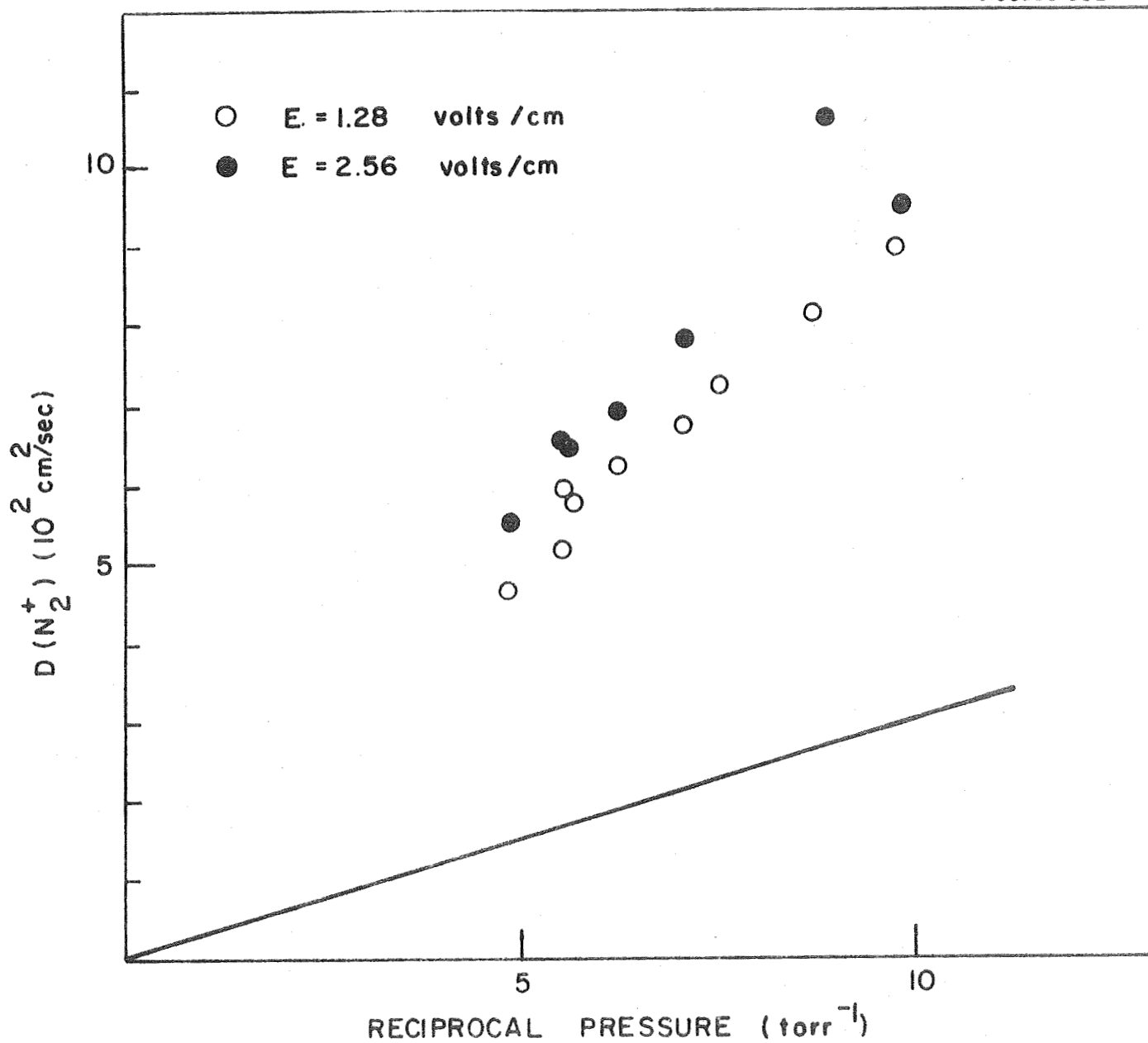


Figure 13: Diffusion coefficients for  $N_2^+$  ( $v = 0$ ) ions in nitrogen. Solid line calculated for thermal ions.

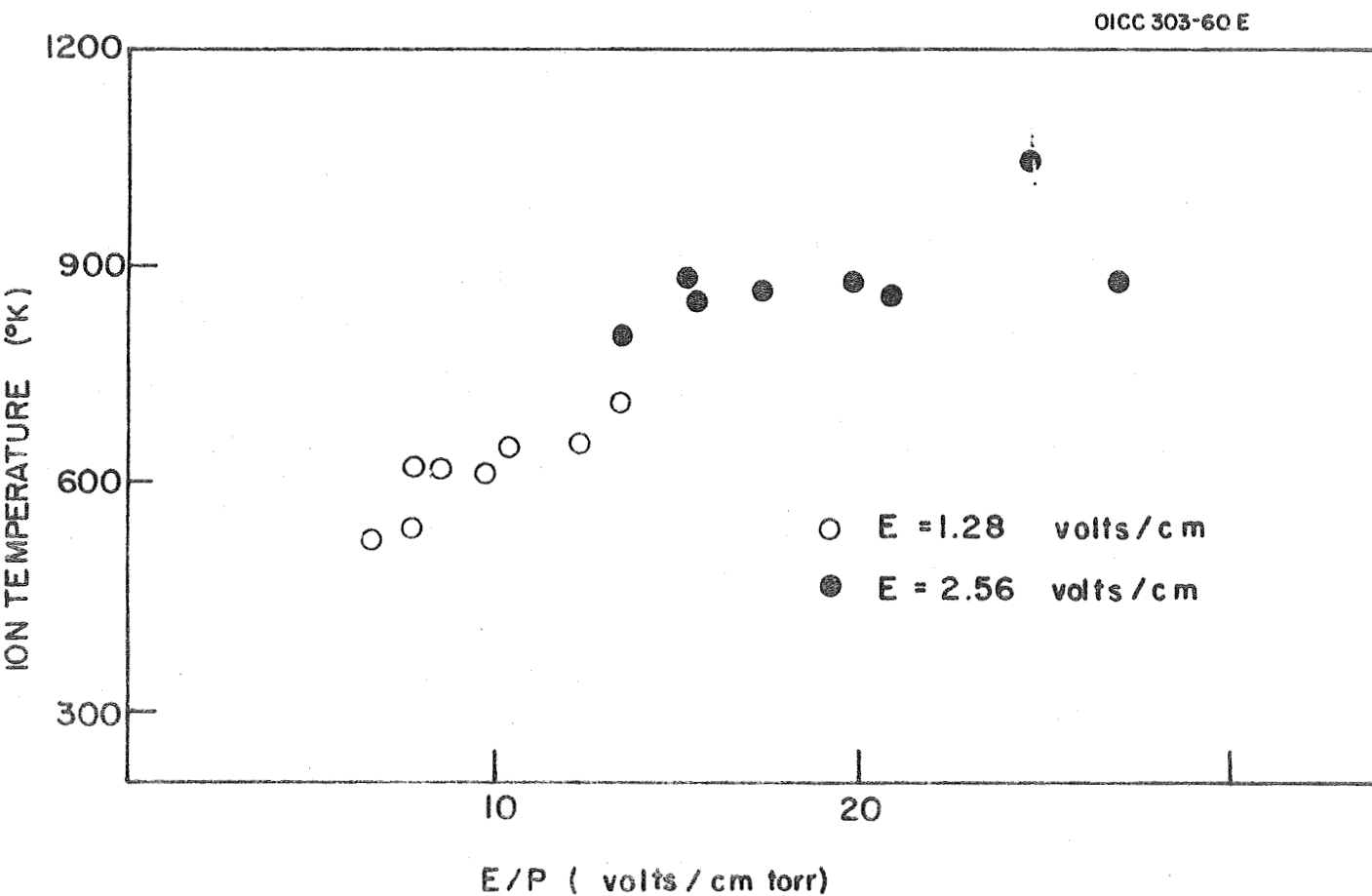
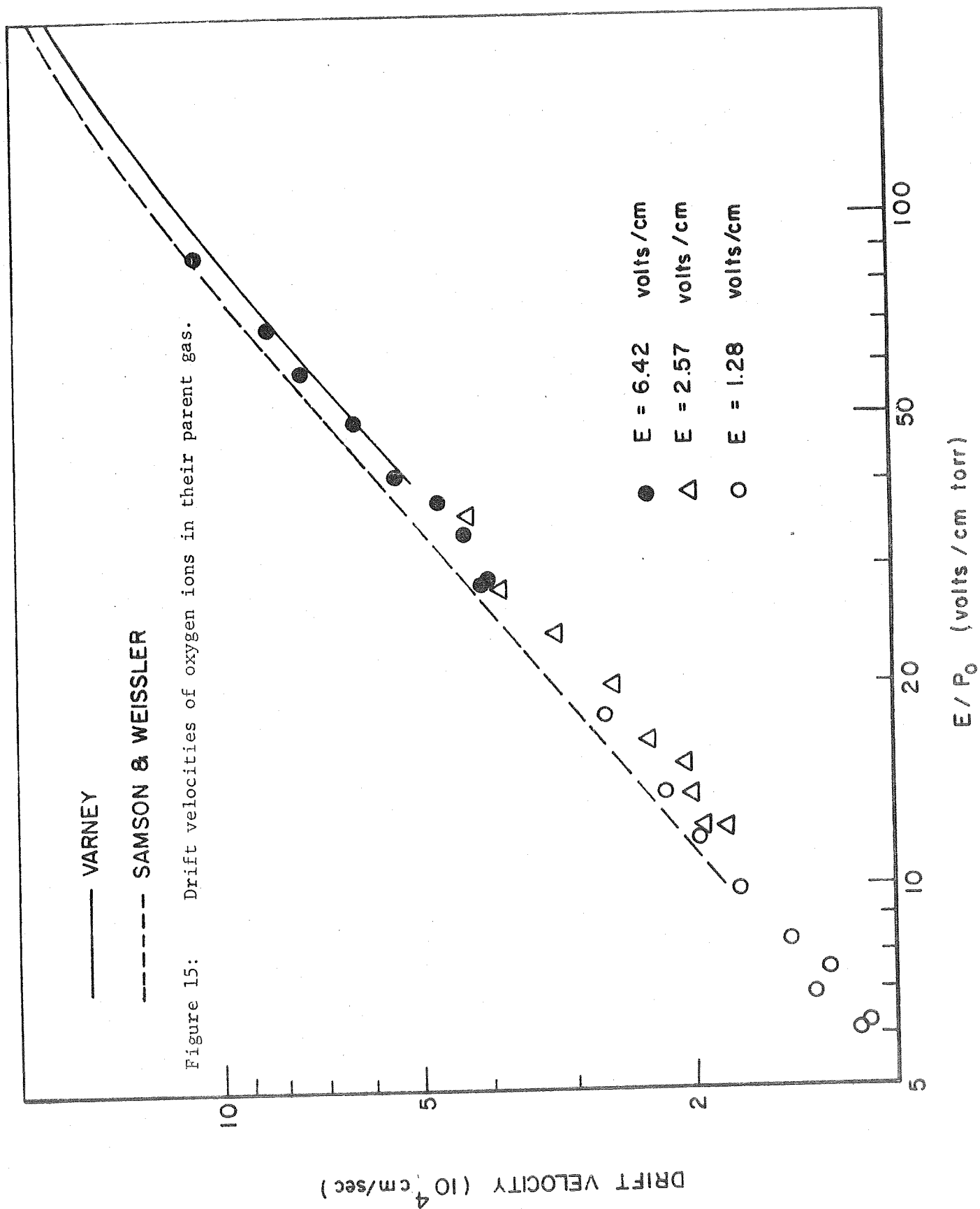


Figure 14: Ion temperature for  $N_2^+$  ( $v = 0$ ) in nitrogen as a function of  $E/P$ .





it appears that the direct photoionization probability for the formation of  $O_2^+$  ( $v = 1$ ) is only a very small fraction of that leading to ground state  $O_2^+$  ions. Unfortunately, a sufficiently strong emission line was not available in the region 1007-1027 $\text{\AA}$  (where  $O_2$  ionization initiates), so that the  $O_2^+$  ( $v = 1$ ) formation could not be positively excluded. However, similar to the previous case ( $N_2^+$ ), an increase in mobility was observed at autoionization features of oxygen. Figure 16 shows that wavelengths at which the  $O_2^+$  residence time in the ion source chamber decreased when the other experimental conditions are kept constant. Each such decrease of residence time (or increase of ion mobility) correlates with an autoionization feature in the absorption spectrum of oxygen in the 900-1000 $\text{\AA}$  wavelength region here investigated. The limited number of strong emission lines available from the light source prevents the demonstration that an increase of mobility is associated with every sufficiently energetic autoionizing feature, but the number of available lines appears to be sufficient to prove the point. The variation in residence times observed is due to the degree of overlap of emission and absorption intensities and the varying ionization efficiencies.

Figures 17 and 18 show the diffusion coefficients and ion temperatures derived for  $O_2^+$  formed at 1007 $\text{\AA}$ . Again it is evident from both groups of data that the ions drifting in the electric field are non-thermal, although the increases in the diffusion coefficient and the ion temperature above thermal values are not as drastic as was found for nitrogen ions.

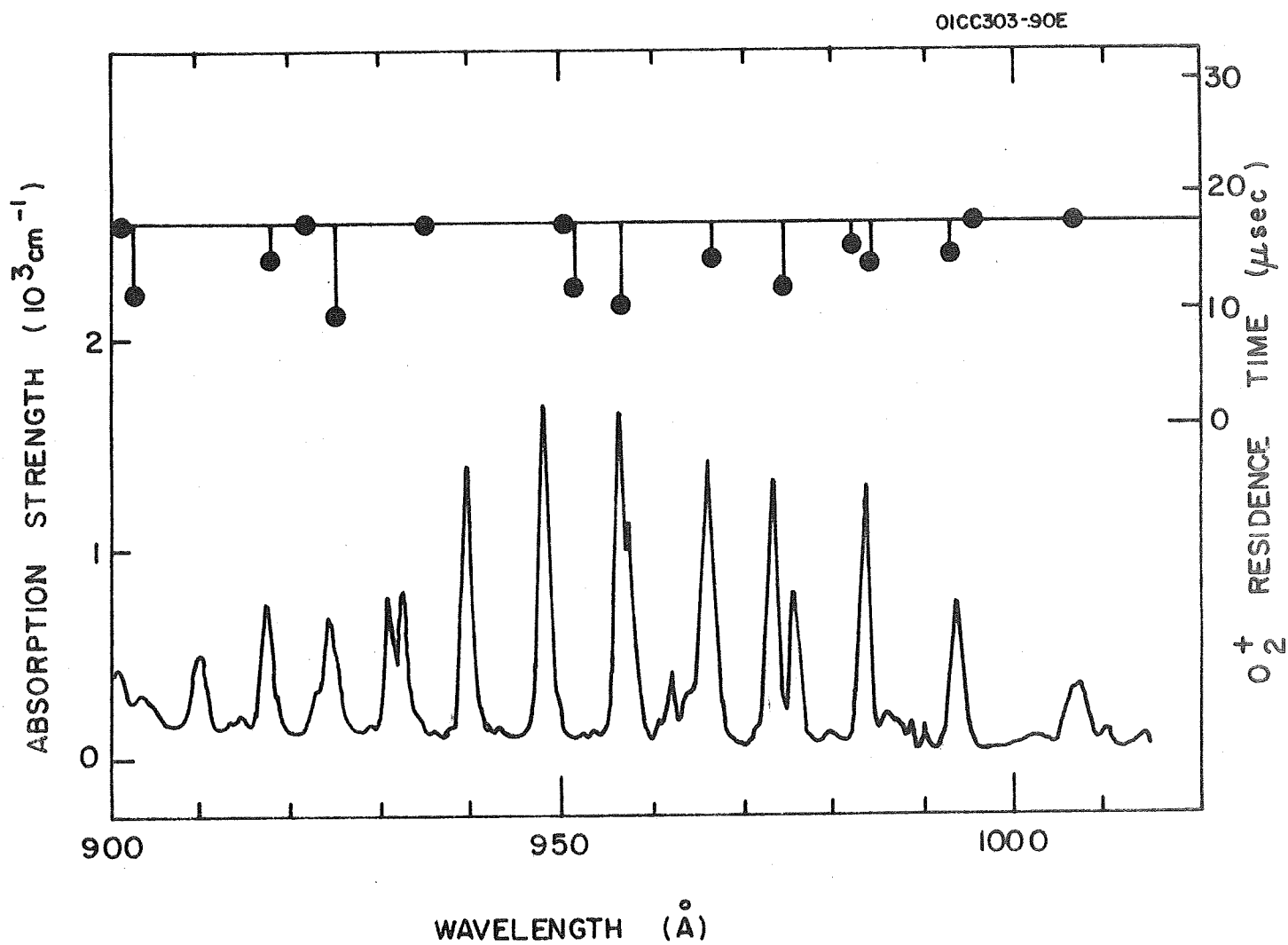


Figure 16: Correlation of oxygen on residence time with autoionization features in the absorption spectrum of oxygen.

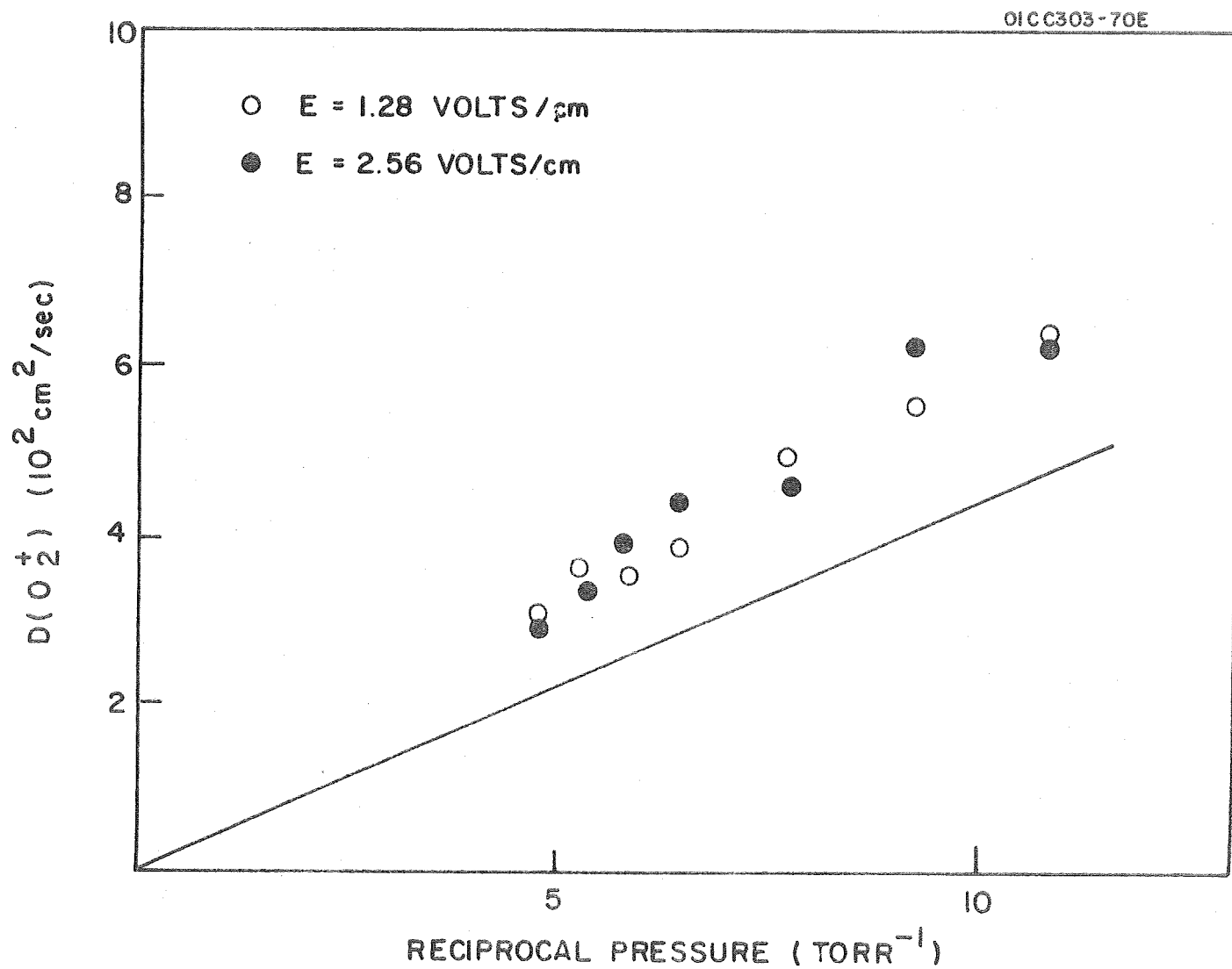


Figure 17: Diffusion coefficients for  $\text{O}_2^+$  ions in oxygen. Solid line calculated for thermal ions.

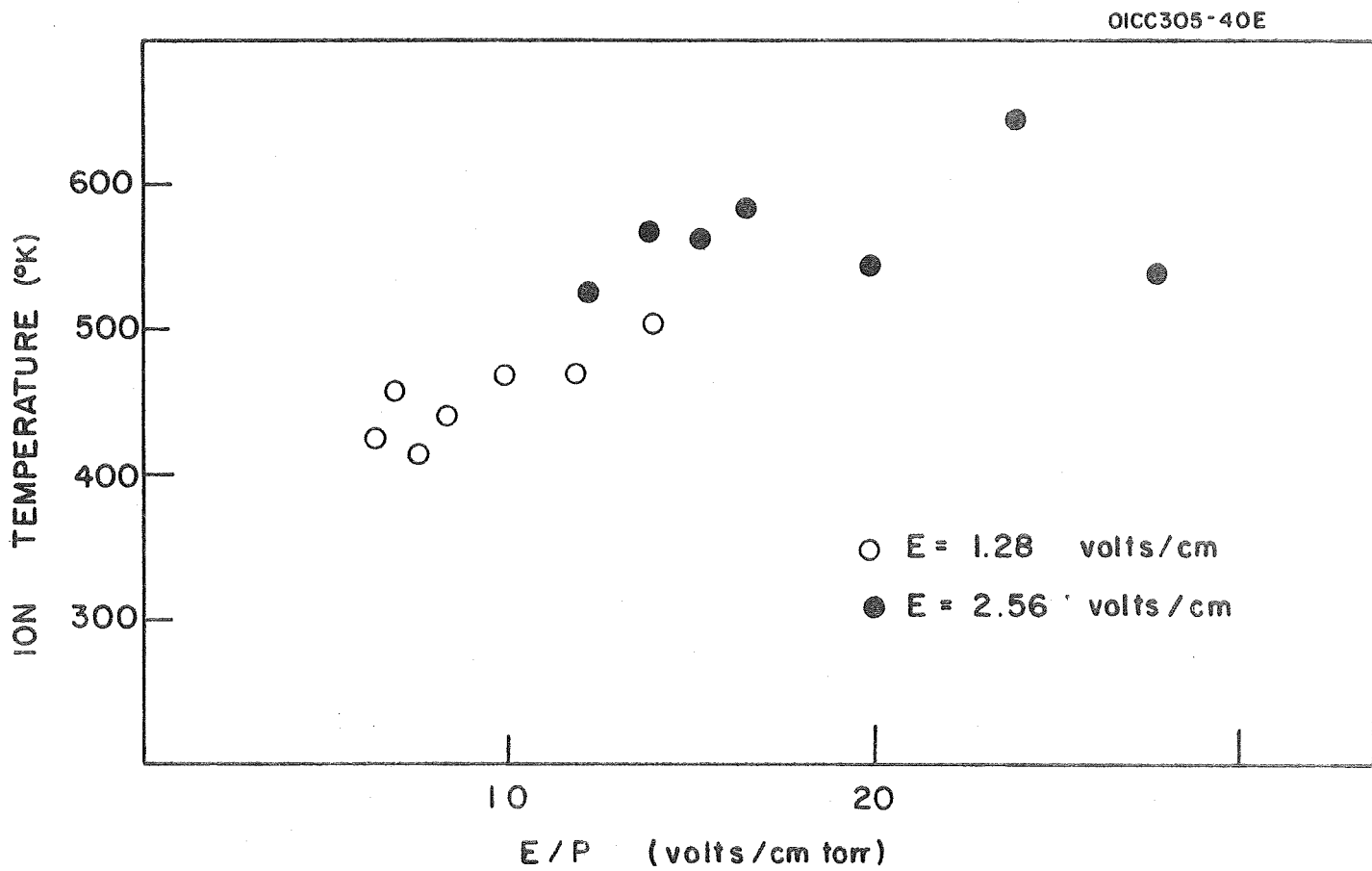


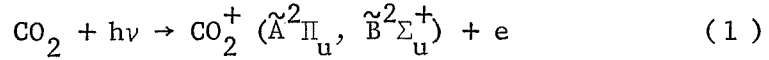
Figure 18: Ion temperature for oxygen ions in oxygen as a function of E/P.

## B. THEORETICAL STUDIES

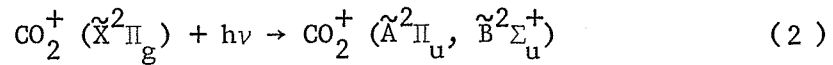
During the current quarterly reporting period a number of theoretical studies were performed in accordance with the tasks specified in the subject work statement. Specifically,  $\text{CO}_2^+$  dayglow on Mars and Venus and spectrography of the lunar atmosphere which are discussed below in the indicated order.

### 1. $\text{CO}_2^+$ Dayglow on Mars and Venus

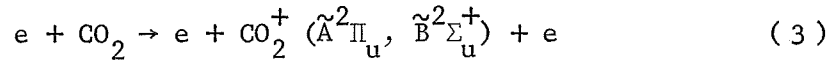
The ground-based observations of Kozyrev<sup>(67)</sup> indicate the occurrence of the  $(\tilde{X}^2\Pi_g - \tilde{A}^2\Pi_u)$  emission bands of  $\text{CO}_2^+$  in the dayglow of Venus<sup>(68)</sup> and the Mariner 6 observations of Barth, et al<sup>(69)</sup> have established that the  $(\tilde{X}^2\Pi_g - \tilde{A}^2\Pi_u)$  and  $(\tilde{X}^2\Pi_g - \tilde{B}^2\Sigma_u^+)$  emission bands are important components of the dayglow of Mars. The excited  $\tilde{A}^2\Pi_u$  and  $\tilde{B}^2\Sigma_u^+$  levels of  $\text{CO}_2^+$  can be populated by direct photoionization of  $\text{CO}_2$  by solar radiation:



by fluorescent scattering of solar radiation by pre-existing  $\text{CO}_2^+$  ion



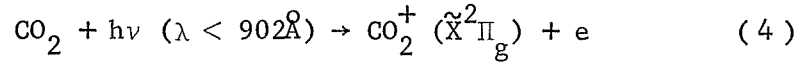
and by simultaneous excitation and ionization of  $\text{CO}_2$  by photoelectron impact:



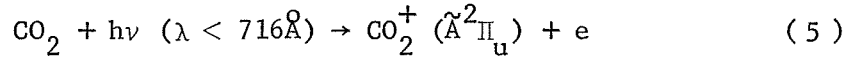
In this paper we shall investigate each of the three mechanisms and calculate their contributions to the  $\text{CO}_2^+$  dayglow on the planets Mars and Venus.

Cross sections for the absorption of radiation by  $\text{CO}_2$  have been measured by Tanaka, Jursa and LeBlanc, <sup>(70)</sup> Tanaka and Ogawa, <sup>(71)</sup> by Nakata, Watanabe and Matsunaga, <sup>(72)</sup> by Cook, Metzger and Ogawa, <sup>(73)</sup> and by Dibeler and Walker. <sup>(74)</sup>

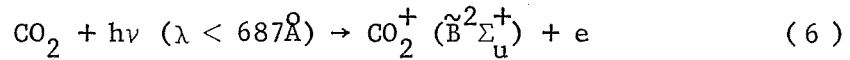
Photons of wavelengths  $\lambda$  shorter than  $902\text{\AA}$  can ionize  $\text{CO}_2$  leaving  $\text{CO}_2^+$  in its ground electronic state:



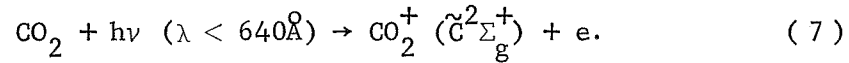
For  $\lambda < 716\text{\AA}$ , it is energetically possible to populate also the first excited state of  $\text{CO}_2^+$  in a photoionizing transition



and for  $\lambda < 687\text{\AA}$  the second excited state



For wavelengths shorter than  $6408\text{\AA}$ , it is possible to produce  $\text{CO}_2^+$  ions in the third excited state



The total photoionization cross sections for  $\text{CO}_2$  have been measured by Nakata, et al, <sup>(72)</sup> by Cairns and Samson, <sup>(75)</sup> by Cook, et al, <sup>(73)</sup> and by Dibeler and Walker <sup>(74)</sup> and the branching ratios appropriate to the  $X^2\Pi_g$ ,  $A^2\Pi_u$ ,  $B^2\Sigma_u^+$ , and  $C^2\Sigma_g^+$  states of  $\text{CO}_2^+$  have been measured by Bahr, Blake, Carver and Kumar. <sup>(76)</sup>

If we assume tentatively that the neutral components of the atmospheres of Mars and Venus are effectively pure  $\text{CO}_2$ , the total rates of population of the electronic levels of  $\text{CO}_2^+$  by photoionization can be calculated directly from the cross section data and the incident solar flux. Our adopted solar flux is based on the 1967 measurements reported by Hinteregger <sup>(77)</sup> for which the solar 10.7 cm flux was  $F_{10.7} = 144$ . We scaled these data appropriately for Mars and Venus and for the 10.7 cm flux  $F_{10.7} = 162$ , adjusted for burst, that was measured at the time of the Mariner 6 flight past Mars.

The results for Mars and for Venus are presented in Tables 4 and 5 respectively for various solar zenith angles,  $Z$ . The table contains the



4  
Table 4

Total production rate of  $\text{CO}_2^+$  states by  
photoionization on Mars in units of  $10^9$   
 $\text{cm}^{-2} \text{sec}^{-1}$  at various solar zenith angles  $z^\circ$ .

$z$	$\tilde{X}^2\Pi_g$	$\tilde{A}^2\Pi_u$	$\tilde{B}^2\Sigma_{ua}^+$	$\tilde{C}^2\Sigma_g^+$
0	6.3	2.8	4.9	1.5
30	5.5	2.4	4.2	1.3
50	4.1	1.8	3.2	0.9
60	3.2	1.4	2.4	0.7
70	2.2	1.0	1.7	0.5
80	1.1	0.5	0.9	0.3

Table 5

Total production rate of  $\text{CO}_2^+$  by photoionization on Venus in units of  $10^9 \text{ cm}^{-2} \text{ sec}^{-1}$  at various solar zenith angles  $z^\circ$ .

$z$	$\tilde{\text{X}}^2\Pi_g$	$\tilde{\text{A}}^2\Pi_u$	$\tilde{\text{B}}^2\Sigma_u^+$	$\tilde{\text{C}}^2\Sigma_g^+$
0	25.0	11.2	19.4	6.5
30	21.7	9.7	16.8	5.7
50	16.1	7.2	12.4	4.2
60	12.5	5.6	9.7	3.3
70	8.6	3.8	6.6	2.2
80	4.4	1.9	3.4	1.1

rates of population in a vertical column. If no deactivation or cascading occurred, the rates would be also the emission intensities in photons  $\text{cm}^{-2} \text{sec}^{-1}$ . Deactivation of the  $\tilde{A}^2\Pi_u$  and  $\tilde{B}^2\Sigma_g^+$  states is negligible since the radiative lifetimes are about  $10^{-7} \text{sec}$  (78-80) but the  $\tilde{C}^2\Sigma_g^+$  state decays to both the  $\tilde{A}^2\Pi_u$  and  $\tilde{B}^2\Sigma_g^+$  states giving rise to emission in the red and infra-red region of the spectrum.

We assume arbitrarily that the branching ratio for cascade into the  $\tilde{A}^2\Pi_u$  and  $\tilde{B}^2\Sigma_g^+$  states is 4:1. The predicted intensities in kilorayleighs of the  $\tilde{X}^2\Pi_g - \tilde{A}^2\Pi_u$  and  $\tilde{X}^2\Pi_g - \tilde{B}^2\Sigma_u^+$  emission systems are given in Table 6.

The rate of population for each molecular ion of  $\text{CO}_2^+$  by fluorescent scattering is given by

$$g = 8.85 \times 10^{-21} I f \lambda^2 \text{sec}^{-1}$$

where  $I$  is the solar continuum intensity at the absorption wavelength  $\lambda^0$  measured in photons  $\text{sec}^{-1} \text{\AA}^{-1}$  and  $f$  is the band oscillator strength. For the lifetime of the  $\tilde{A}^2\Pi_u$  state, Schwenker (78) has measured a value of  $1.39 \times 10^{-7} \text{sec}$  and Hesser and Dressler (81) and Hesser (80) a value of  $1.1 \times 10^{-7} \text{sec}$ . The values are in harmony with that derived by Anton (79) from pressure quenching measurements. The system oscillator strength corresponding to a lifetime of  $1.1 \times 10^{-7} \text{sec}$  is  $f = 1.5 \times 10^{-2}$ . Taken in conjunction with the relative probabilities of Poulizac and Dufay (82) and the solar fluxes at the band heads, this oscillator strength gives a  $g$  value for the  $\tilde{A}^2\Pi_u$  population of  $1.1 \times 10^{-2}$  at Mars and  $4.9 \times 10^{-2}$  at Venus.

Table 6

Predicted intensities in kilorayleighs of the  $\tilde{X}^2\Pi_g - \tilde{A}^2\Pi_u$  and  $\tilde{X}^2\Pi_g - \tilde{B}^2\Sigma_u^+$  band systems resulting from photoionization on Mars and Venus at various solar zenith angles  $z^\circ$ .

z	Mars		Venus	
	$\tilde{A}^2\Pi_u$	$\tilde{B}^2\Sigma_u^+$	$\tilde{A}^2\Pi_u$	$\tilde{B}^2\Sigma_u^+$
0	4.0	5.2	15.8	20.5
30	3.5	4.5	13.7	17.8
50	2.6	3.4	10.2	13.2
60	2.0	2.6	7.9	10.3
70	1.4	1.8	5.4	7.0
80	0.7	0.9	2.7	3.6

For the  $\tilde{B}^2\Sigma_u^+$  state of  $\text{CO}_2^+$ , Hesser and Dressler<sup>(81)</sup> and Hesser<sup>(80)</sup> have measured a lifetime of  $1.19 \times 10^{-7}$  sec consistent with an absorption oscillator strength of  $5.3 \times 10^{-3}$ . The corresponding g-value at Mars is  $1.2 \times 10^{-3}$  and the g- value at Venus is  $5.2 \times 10^{-3}$ . In making these estimates of scattering efficiencies, Fraunhofer absorption has been ignored.

If we assume tentatively that the ionic components of the atmospheres are pure  $\text{CO}_2^+$ , the total rates of emission of the two  $\text{CO}_2^+$  band systems can be calculated directly from the measured electron densities. For Mars, the total electron content derived from Mariner 4 occultation data was about  $4.2 \times 10^{11} \text{ cm}^{-2}$  for a solar zenith angle of  $67^\circ$ <sup>(83, 84)</sup> and from Mariner 6 data it was about  $1.2 \times 10^{12} \text{ cm}^{-2}$  for a solar zenith angle of  $56^\circ$ <sup>(85)</sup>. For Venus the total electron content derived from Mariner 5 occultation data was about  $1.6 \times 10^{12} \text{ cm}^{-2}$  for a solar zenith angle of  $33^\circ$ <sup>(86)</sup>.

The measured Venus ionization profile is consistent with a pure  $\text{CO}_2$  atmosphere and dissociation recombination of  $\text{CO}_2^+$ <sup>(87)</sup>. We have extended the equilibrium calculations of McElroy<sup>(87)</sup> to other zenith angles and we obtain the total ionization contents of Table 7, scaled linearly to that observed at  $33^\circ$ .

We adopt a similar model for Mars, but scaled linearly to the observed total electron contents at  $56^\circ$  or  $67^\circ$ . The corresponding ionization contents on Mars at various solar zenith angles are included in Table 7. The linear scaling procedure is an arbitrary one.

Table 7

Total ionization content in  $10^{11} \text{ cm}^{-2}$  on Mars  
and Venus at various solar zenith angles  $z^\circ$ .

Z	Mars		Venus
	Mariner 4	Mariner 6	Mariner 5
0	6.4	15.1	17.7
30	6.0	14.1	16.8
50	5.2	12.4	14.7
60	4.8	11.2	13.2
70	3.9	9.4	11.2
80	3.0	7.3	8.4

The contributions to the  $\tilde{X}^2\Pi_g - \tilde{A}^2\Pi_u$  and  $\tilde{X}^2\Pi_g - \tilde{B}^2\Sigma_u^+$  emission intensities from fluorescent scattering by  $\text{CO}_2^+$  are given in kilorayleighs in Table 8.

The photoelectrons produced by photoionization lose energy through excitation and ionization of  $\text{CO}_2$  and by elastic collisions with the ambient electrons. Some fraction of the ionizations leaves  $\text{CO}_2^+$  in excited states. Precise predictions would involve detailed studies of the energy degradation of the photoelectrons of the kind carried out for the earth by Green and Barth<sup>(88)</sup> and by Dalgarno, McElroy and Stewart.<sup>(89)</sup> We can easily demonstrate however that photoelectron impact is a comparatively small source of population of the  $\tilde{A}^2\Pi_u$  and  $\tilde{B}^2\Sigma_u^+$  states of  $\text{CO}_2^+$  on Mars and Venus.

The thresholds for ionization to the  $\tilde{X}^2\Pi_g$ ,  $\tilde{A}^2\Pi_u$  and  $\tilde{B}^2\Sigma_u^+$  states occur at respectively 13.8 eV, 17.3 eV and 18.1 eV. The energy flux of photoelectrons with energies greater than 17.3 eV is about  $3.8 \times 10^{11}$  eV  $\text{cm}^{-2} \text{sec}^{-1}$  on Mars and about  $1.5 \times 10^{12}$  eV  $\text{cm}^{-2} \text{sec}^{-1}$  on Venus for the sun at zenith. For fast electrons absorbed by  $\text{CO}_2$  the mean energy per ion pair is about 35 eV, a value which must increase ultimately with decreasing initial electron energy. Thus, the number of ionizations produced by electrons with energies in excess of 17.3 eV does not exceed  $1.1 \times 10^{10} \text{cm}^{-2} \text{sec}^{-1}$  on Mars and does not exceed  $4.3 \times 10^{10} \text{cm}^{-2} \text{sec}^{-1}$  on Venus. According to McConkey, Burns and Woolsey<sup>(90)</sup> the excitation functions of the  $\tilde{A}^2\Pi_u$  and  $\tilde{B}^2\Sigma_u^+$  states are similar in shape to the total ionization function,<sup>(91)</sup> the ratios being approximately 1/5 and 1/15

Table 8

Predicted intensities in kilorayleighs of the  $\tilde{X}^2\Pi_g - \tilde{A}^2\Pi_u$  and  $\tilde{X}^2\Pi_g - \tilde{B}^2\Sigma_u^+$  band systems resulting from fluorescent scattering on Mars and Venus at various solar zenith angles  $z^\circ$ . The  $\text{CO}_2^+$  contents are based upon the Mariner 5 and Mariner 6 data.

z	Mars		Venus	
	$\tilde{A}^2\Pi_u$	$\tilde{B}^2\Sigma_u^+$	$\tilde{A}^2\Pi_u$	$\tilde{B}^2\Sigma_u^+$
0	15.9	1.8	86.7	8.8
30	15.3	1.6	82.3	8.4
50	13.9	1.5	72.0	7.3
60	12.3	1.3	64.6	6.6
70	10.2	1.0	55.2	5.7
80	7.6	0.9	41.1	4.2



respectively. The corresponding upper limits to the  $\tilde{X}^2_{\Pi_g} - \tilde{A}^2_{\Pi_u}$  and  $\tilde{X}^2_{\Pi_g} - \tilde{B}^2_{\Sigma_u^+}$  emission intensities are respectively 2 kR and 700 R on Mars and 9 kR and 3 kR on Venus, all values referring to  $Z = 0^\circ$ . The actual intensities may be of the order of half the upper limits. The estimated intensities from photoelectron impact are given in Table 9 for various solar zenith angles.

Table 10 summarizes the contributions from the three sources for Mars at a solar zenith angle of  $30^\circ$ . Photoionization and fluorescence scattering are important sources for both transitions. Photoionization is more important for one system and fluorescence scattering for the other. Fluorescence scattering assumes a larger role for both planets with increasing solar zenith angle and it is relatively more important on Venus than on Mars.

Photoelectron impact contributes not more than 5 percent to either transition on either planet at any solar zenith angle. Barth, et al.<sup>(69)</sup> have remarked that their Mars spectrum is similar to that produced in the laboratory by the bombardment of  $\text{CO}_2$  with electrons of 20 eV energy. According to the cross section data of McConkey, et al.,<sup>(90)</sup> the ratio of system intensities produced by 20 eV electrons is somewhat greater than 3 consistent with our predicted ratio on Mars at  $30^\circ$  of 3.1, produced by a combination of photoionization and fluorescence scattering.

Our ratio refers to the total intensities, whereas the measurements of Barth, et al.<sup>(69)</sup> give the intensities above particular altitudes. If we have correctly identified the excitation mechanisms, the ratio of the

Table 9

Estimated\* intensities in kilorayleighs of the  $\tilde{X}^2\Pi_g - \tilde{A}^2\Pi_u$  and  $\tilde{X}^2\Pi_g - \tilde{B}^2\Sigma_u^+$  band systems resulting from photoelectron impacts on Mars and Venus at various solar zenith angles  $z^\circ$ .

Z	Mars		Venus	
	$\tilde{A}^2\Pi_u$	$\tilde{B}^2\Sigma_u^+$	$\tilde{A}^2\Pi_u$	$\tilde{B}^2\Sigma_u^+$
0	1.1	0.4	4.3	1.4
30	0.9	0.3	3.7	1.2
50	0.7	0.2	2.8	0.9
60	0.5	0.2	2.1	0.7
70	0.4	0.1	1.5	0.5
80	0.2	0.1	0.7	0.2

\*Upper limits are obtained by doubling the entries. The ratio of any pair of entries is much more accurate than the individual entries.

Table 10

Theoretical intensities in kilorayleighs of the  $\tilde{X}^2\Pi_g - \tilde{A}^2\Pi_u$  and  $\tilde{X}^2\Pi_g - \tilde{B}^2\Sigma_u^+$  band systems resulting from photoionization, fluorescence scattering and photoelectron impact on Mars at  $30^\circ$  solar zenith angle.

System	$\tilde{X}^2\Pi_g - \tilde{A}^2\Pi_u$	$\tilde{X}^2\Pi_g - \tilde{B}^2\Sigma_u^+$
Photoionization	3.5	4.5
Fluorescence scattering	15.3	1.6
Photoelectron impact	0.9	0.3
Total	19.7	6.4

intensity of the  $\tilde{X}^2\Pi_g - \tilde{A}^2\Pi_u$  system to that of the  $\tilde{X}^2\Pi_g - \tilde{B}^2\Pi_u^+$  system should increase with increasing altitude because photoionization decreases with the scale height of the neutral atmosphere and fluorescent scattering decreases with the scale height of the ionized component (if the major ion remains  $\text{CO}_2^+$ ). A detailed study of the Mars data of Barth, et al<sup>(69)</sup> may provide a test of the solar wind model of Cloutier, McElroy and Michel.<sup>(92)</sup>

The increasing importance of fluorescent scattering with increasing altitude should be reflected also in a changing vibrational distribution within the  $\tilde{X}^2\Pi_g - \tilde{A}^2\Pi_u$  electronic transition.

Measurements of photoionization cross sections of  $\text{CO}_2$  in which the individual vibrational levels of the product electronic state are resolved have been carried out by Turner and May<sup>(93)</sup> and by Spohr and Puttkamer<sup>(94)</sup> for a wavelength of  $584\text{\AA}$ . The values for the  $\tilde{A}^2\Pi_u$  state decrease more slowly with increasing  $v'$  than do the theoretical Franck-Condon factors of Sharp and Rosenstock.<sup>(95)</sup>

Contributions to photoionization from autoionizing levels of  $\text{CO}_2$  are significant in the region between  $830$  and  $600\text{\AA}$ <sup>(74)</sup> and the vibrational populations in the atmosphere are modified by cascading. Despite the uncertainties, we proceed on the assumption that the  $584\text{\AA}$  ratios of Table 11 give the relative rates of population of the different vibrational levels by photoionization in the atmospheres of Mars and Venus.

The relative efficiencies with which fluorescent scattering populates the individual vibrational levels of the  $\tilde{A}^2\Pi_u$  state can be computed

Table 11

Relative probabilities for populating vibrational levels  $v'$  of the  $\tilde{A}^2\Pi_u$  state of  $\text{CO}_2^+$  by photoionization, by fluorescent scattering and by electron impact.

$v'$	Photoionization	Fluorescent scattering	Electron impact
0	0.08	0.30	0.09
1	0.18	0.35	0.21
2	0.20	0.25	0.20
3	0.22	0.07	0.23
4	0.16	0.015	0.21
5	0.12	0.005	0.06

from the solar flux intensities and the Franck-Condon factors for the  $\tilde{X}^2\Pi_g(v'' = 0) - \tilde{A}^2\Pi_u(v')$  transitions. The results are included in Table 11 as are the approximate relative efficiencies for electron impact that follow from the data of Nishimura<sup>(96)</sup> and McConkey, et al.<sup>(90)</sup>

Individual band intensities resulting from the three sources of excitation can be calculated approximately by combining Table 11 with the relative transition probabilities of Poulizac and Dufay.<sup>(82)</sup> The relative band intensities are listed in Table 12 together with the approximate wavelengths of the mean band heads for  $^2\Pi_{1/2}$  and  $^2\Pi_{3/2}$  final states. Table 12 shows that in the altitude region where  $CO_2^+$  is the major positive ion bands originating in  $v' = 0$  and 1 becomes relatively more intense with increasing altitude than bands originating in  $v' = 2$ .

Molecular nitrogen may be a minor constituent of the atmospheres of Mars and Venus. Of the many emission band systems, the appearance of which would establish the presence of  $N_2$ , the 3914 Å band of the first negative system of  $N_2^+$  may be the most sensitive. The  $\tilde{B}^2\Sigma_u^+$  level of  $N_2^+$  can be excited by the same three mechanisms that we have studied for the  $CO_2^+$  emissions.

The  $N_2^+$  ions produced by photoionization can be removed by dissociative recombination



with a rate coefficient of about  $3 \times 10^{-7} \text{ cm}^3 \text{ sec}^{-1}$ <sup>(97)</sup> and by conversion into  $CO_2^+$  through the reaction



Table 12

Approximate relative intensities and wavelengths in Å of the bands of the  $\tilde{X}^2\Pi_g - \tilde{A}^2\Pi_u$  transition of  $\text{CO}_2^+$  produced by (1) photoionization of  $\text{CO}_2$ , (2) fluorescent scattering by  $\text{CO}_2^+$  and (3) electron impact of  $\text{CO}_2$ .

$v' - v''$		0	1	2	3	4	5
0	(1)	0.19	0.58	0.58	0.24	0.05	0.01
	(2)	0.69	1.12	0.72	0.08	0.00	0.00
	(3)	0.20	0.67	0.58	0.26	0.05	0.01
	$\lambda$ (Å)	3508	3374	3250	3136	3031	2935
1	(1)	0.27	0.14	0.22	0.33	0.27	0.13
	(2)	0.96	0.28	0.27	0.10	0.03	0.00
	(3)	0.29	0.17	0.22	0.33	0.36	0.07
	$\lambda$ (Å)	3669	3523	3390	3267	3154	3046
2	(1)	0.15	0.23	0.39	0.14	0.27	0.16
	(2)	0.54	0.46	0.49	0.05	0.03	0.01
	(3)	0.16	0.28	0.39	0.15	0.36	0.08
	$\lambda$ (Å)	3845	3686	3704	3553	3420	3300
3	(1)	0.08	0.34	0.08	0.29	0.11	0.02
	(2)	0.30	0.68	0.10	0.09	0.01	0.00
	(3)	0.09	0.40	0.08	0.30	0.15	0.01
	$\lambda$ (Å)	4038	3863	3704	3553	3420	3300
4	(1)	0.04	0.23	0.20	----	0.13	0.06
	(2)	0.15	0.46	0.40		0.01	0.00
	(3)	0.04	0.28	0.20		0.15	0.03
	$\lambda$ (Å)	4264	4059	3883		3573	3440
5	(1)	----	0.07	0.16	0.15	----	----
	(2)		0.14	0.32	0.05		
	(3)		0.09	0.16	0.16		
	$\lambda$ (Å)		4301	4102	3925		

which has a rate coefficient of  $9 \times 10^{-10} \text{ cm}^3 \text{ sec}^{-1}$ .<sup>(98)</sup> For illustrative purposes we have adopted model atmospheres for Mars containing 9 percent  $\text{N}_2$  and 91 percent  $\text{CO}_2$  with an exospheric temperature of  $487^\circ$ .<sup>(87)</sup> The atmosphere is assumed to be either completely mixed at all altitudes or such that diffusive separation begins at 120 km. The total abundance of  $\text{N}_2^+$  ions lies in the range from  $10^9$  to  $10^8 \text{ cm}^{-2}$  and the fluorescent scattering intensity on Mars lies between 20 Rayleighs and 2 Rayleighs.

The contribution from simultaneous excitation and ionization in a direct photoionization process can be computed straightforwardly. It is 120 Rayleighs for the diffusive model and 70 Rayleighs for the mixed model.

The contribution from photoelectron impact can be estimated using arguments similar to those mentioned previously. It is unlikely to exceed 50 Rayleighs for the diffusively separated atmosphere or 20 Rayleighs for the mixed atmosphere.

The intensity of  $3914 \text{ \AA}$  emission that we predict for a  $\text{CO}_2 - \text{N}_2$  composition ratio of ten is accordingly two or three hundred Rayleighs for the entire atmosphere. The predicted intensity could be substantially reduced by the presence of a lighter constituent such as atomic oxygen.

## 2. Spectrography of the Lunar Atmosphere

The proposed experimental investigation involves the employment of a compact, light weight, automatically operating spectrograph on the



lunar surface to photographically record signature spectra of resonance (and/or fluorescence) scattering from solar illuminated lunar atmospheric species (or LEM contaminant species). The relatively high sensitivity achievable by the proposed instrumentation (ppm or less) and the extensive spectral region included in the measurement program ( $\lambda\lambda$  500 to 4500 $\text{\AA}$ ) result in the conduct of a survey experiment on establishing the presence or absence of specific lunar atmospheric species.

The proposed experiment is ideally suited for operation on the lunar surface. First, the spectrograph film format results in simultaneous integration over each individual spectral resolution so that the required broad spectral range can be covered at full sensitivity. In addition, since the proposed instrumentation encompasses a self-contained operational entity, power, telemetry, data sharing, interference, etc. characteristics need be considered in the conduct of the experiment. Upon comparison of the overall capabilities of the experiment performed at a remote observation platform to the suggested lunar surface program, the following advantages are apparent: (a) the experimental conditions remain essentially constant throughout the viewing time, i.e., the incident solar flux, the ambient background, column of specific species (signal source), the viewing position and angle, etc.; (b) species number densities are maximum at the surface so that the resultant  $\text{cm}^2$ -column count is optimized. This feature is especially evident in the detection of

relatively heavy constituents, such as krypton, xenon, argon, etc. (which have relatively low scale heights from a remote platform); (c) the required astronaut activity is simple, minimum, and vital; (d) the selection of the surface-based viewing geometry is extremely flexible; (e) the instrumentation can be located in the vicinity of the LEM vehicle so that an opportunity exists for detecting fuel contaminants and measuring their inventories as a function of time.

The data acquired from the indicated experiments can be employed in the identification of dominant lunar atmospheric source and sink functions as well as the pertinent mechanisms involved. Additionally, the spectrographic data can be correlated with other Apollo mission measurement program results, i.e., solar wind indicators, seismology, meteoric impact, etc.

Several observational experimental programs have been conducted previously to ascertain the existence, constituency, and extent of a lunar atmosphere. A concise summary of these results involving a broad variety of experimental techniques has been presented by Sytinskaya.<sup>(99)</sup> Highly sensitive experiments were performed by Lyot and Dollfus<sup>(100)</sup> and Dollfus<sup>(101)</sup> who were searching for the effects of Rayleigh scattering from a lunar atmosphere located just beyond the horns of a crescent moon. They employed a coronagraph to minimize instrumental scattering of disk light and took advantage of the polarization characteristics of Rayleigh scattered light. Their results indicated that the total surface number density of the lunar atmosphere must be less than  $10^{-9}$  that of the sea level terrestrial atmosphere (i.e.,  $< 3 \times 10^{10} \text{ cm}^{-3}$ ).

On the basis of the results of a radio refraction experiment involving lunar occultation of the Crab Nebula, Elsmore<sup>(102)</sup> deduced that a surface electron density of about  $10^3 \text{ cm}^{-3}$  in excess of that of the surrounding interplanetary medium obtains for the lunar atmosphere. On the basis of an extrapolation of these data, he suggested a new upper limit value for neutral species at the lunar surface of only about  $2 \times 10^{-13}$  earth atmospheres.

Herzberg<sup>(103)</sup> suggested that the observation of characteristic fluorescences for specific species offered a sensitive species detection possibility. Subsequently, Kuiper<sup>(104)</sup> established that lunar atmospheric  $\text{SO}_2$  amounted to less than  $7 \times 10^{-10}$  earth atmospheres on the basis of the absence of absorption bands on observed lunar disk light. Recently, Marmo and Engelman<sup>(105)</sup> defined a manned orbital experiment involving the observation of resonance radiations from solar illuminated neutral or ionic constituents in the lunar atmosphere. It was demonstrated both that a number of potentially important resonance lines occurred in the visible spectral region and that a meaningful experiment could be performed at an earth-based observatory.

Finally, Marmo and Manring<sup>(106)</sup> utilized the Sacramento Peak coronagraph to image, occult, and track the lunar disk in an attempt to observe atmospheric contents of Na I, Ca I, and Ca II along the lunar limb. The results indicated upper limit values for these species of about  $10^9 / \text{cm}^2$ -column.

For the purposes of the proposed experiment, the state of present development over the entire field of activity is sufficient so that no

new technology is envisioned. For example, the required astronaut activity is straightforward though vital in nature, thus requiring minimum effort and instruction. Additionally, a prototype of the suggested instrumentation has been employed in a number and variety of high altitude rocket experimental programs designed to measure vacuum ultraviolet (VUV) airglow in the earth atmosphere. For the present application, the only requirements involve simple instrumental size reduction, operational compatibility with the lunar environment, and the design of a removable film cassette for subsequent return to earth.

The Apollo mission experiment discussed herein involves the employment of a simple, light weight, automatically operated, dual spectrograph designed to perform observations in two spectral regions, i.e.  $\lambda\lambda$  2500-4500Å and  $\lambda\lambda$  500-2500Å. The experiment is to be performed on the lunar surface in the protective shade of the LEM vehicle. The astronaut will initiate the pre-programmed experimental sequence of tasks which the instrument is designed to perform automatically. Subsequent to automatic shutdown, the astronaut will remove the capsule containing the roll film spectroscopic data for return to earth for development, data reduction, and analysis and interpretation. This initial experiment should be considered in terms of a general survey in that an extensive spectral region will be covered wherein the presence or absence of signals owing to resonance scattering from solar illuminated species in the lunar atmosphere can be detected with relatively high sensitivity. The recommended experimental technique will yield data which can represent meaningful

inputs to the definition of relevant mechanisms producing the measured species number densities. The proposed experiment will be performed with existing state-of-the-art instrumentation and minimum, although vital, astronaut activity. The experimental objectives and results can be applied and correlated with other experiments performed under the Apollo mission program. Finally, on the basis of the derived experimental results, the location of a permanent astronomical airglow observing site on the lunar surface may be indicated which would operate essentially continuously and in direct communication with earth.

A meaningful experiment designed to determine the constituency and extent of the lunar atmosphere must operate within the constraints of the accepted upper limit values of  $10^6 \text{ cm}^{-3}$  and  $10^3 \text{ cm}^{-3}$  for total surface number densities for neutral and ionic species, respectively. (99,102) Within these limits, several theoretical investigations have been performed, the results of which are described in the literature (105,107-110) so that a detailed discussion is not included herein. Suffice it to note that a number of representative possible lunar atmospheric constituents have been selected for the purposes of illustrating the present experimental capability and its applicability to the present state of knowledge. This species tabulation is presented in column 1 of Table 13 with corresponding relevant resonance wavelengths. Present theory does not allow one to estimate the inventories of the individual species which may be resident in the lunar atmosphere which represents the general rationale for the importance of the proposed general survey experiment. In lieu of this specific knowledge, the expected signal brightness values in Rayleighs

TABLE 13

## SELECTED LUNAR ATMOSPHERIC SPECIES, POSSIBILITIES AND ASSOCIATED SPECTROGRAPHIC DETECTION CAPABILITIES

Species	$\lambda(\text{\AA})$	Expected Signal Brightness ( $\phi$ , Rayleighs) for Surface Number Density ( $n_0, \text{cm}^{-3}$ )=1	Minimum Detectable $n_0$ - Value for $\phi=1\text{R}$	Major Sources of Con- stituent in Lunar Atmosphere
<u><math>\lambda\lambda</math> 2500-4500<math>\text{\AA}</math></u>				
Ca I	4227	9.3(0) Rayleigh	1.1(-1) $\text{cm}^{-3}$	SW-ME
***K I	4044	5.9(0)	1.7(-1)	SW-ME
Ca II	3934	1.2(1)	8.3(-2)	SW-ME
Fe I	3441	6.1(-1)	1.6(0)	SW-ME
Ni I	3370	6.5(0)	1.5(-1)	SW-ME
Ti I	3342	3.4(1)	2.9(-2)	SW-ME
***Na I	3302	2.6(0)	3.9(-1)	SW-ME
***Li I	3233	3.8(0)	2.6(-1)	SW-ME
Al I	3082	8.7(0)	1.1(-1)	SW-ME
Mg I	2852	1.2(1)	8.3(-2)	SW-ME
Mg II	2796	3.8(0)	2.6(-1)	SW-ME
Fe II	2599	2.1(0)	4.8(-1)	SW-ME
Si I	2514	6.3(-1)	1.6(0)	SW-ME
<u><math>\lambda\lambda</math> 500-2500<math>\text{\AA}</math></u>				
C I	1657	1.4(-2)	7.1(1)	SW-ME-VO-FC
Xe I	1470	9.2(-5)	1.1(4)	SW-RA-PR
O I	1304	9.0(-5)	1.1(4)	SW-ME-VO-FC
H I	1216	4.9(-1)	2.0(0)	SW-VO-FC
N I	1200	2.6(-4)	3.8(3)	SW-ME-FC
Kr I	1165	4.9(-6)	2.0(5)	SW-RA
Ar I	1048	1.1(-5)	9.1(4)	SW-RA-PR
Ne I	736	4.0(-6)	2.5(5)	SW
He I	584	1.8(-4)	5.6(3)	SW-RA

\* number in parentheses denotes power of ten, i.e.  $1.0(2) = 1.0 \times 10^2$

\*\*SOURCE FUNCTIONS:

SW, solar wind; ME, meteoric bombardment; VO, volcanic activity; RA, radioactive decay;  
PR, original atmospheric residua; FC, fuel contaminants

\*\*\*the tabulated wavelengths pertain to second resonance lines of the species; the first resonance lines are K I (7665), Na I (5890), Li I (6708).

(where 1 Rayleigh =  $10^6$  photons/cm<sup>2</sup> sec emitted in  $4\pi$  steradians), are tabulated in column 3 of Table 13 for surface number densities,  $n_o$ , of only 1 cm<sup>-3</sup> for the individual constituents. This sensitivity is expressed in an alternative fashion in column 4 of Table 13 in terms of minimum detectable  $n_o$ -values for an assumed detectability of 1.0 Rayleigh. Finally, the last column of Table 13 lists the major possible source functions of the individual constituents considered as extracted from the literature. (101-105)

The above tabulation has been separated into two spectral categories, i.e.  $\lambda\lambda$  2500 to 4500Å, and  $\lambda\lambda$  500 to 2500Å, since the proposed investigation will be performed using two spectrograph systems consistent with this spectral dichotomy. The instrumentation is discussed in greater detail in the following section where it is demonstrated that system detectabilities can be achieved which correspond to signal intensities between about 1 to 10 Rayleighs. On this basis, the data in Table 13 indicate that this instrumentation capability will result in high probability of detecting and identifying (or alternatively, establishing meaningful upper limit surface density values) a large number and variety of possible lunar atmospheric species.

The proposed experiment is predicated on the employment of a simple design spectrograph of reasonable resolution which is both compact and light weight. An optimum design for the present experimental purpose is shown in Figure 19 which illustrates the optical configuration of a simple normal incidence spectrograph. In Figure 19, the housing geometry is indicated in order to illustrate the compact nature of the resultant spectrograph. The entrance slit, grating and plate holder positions indicated

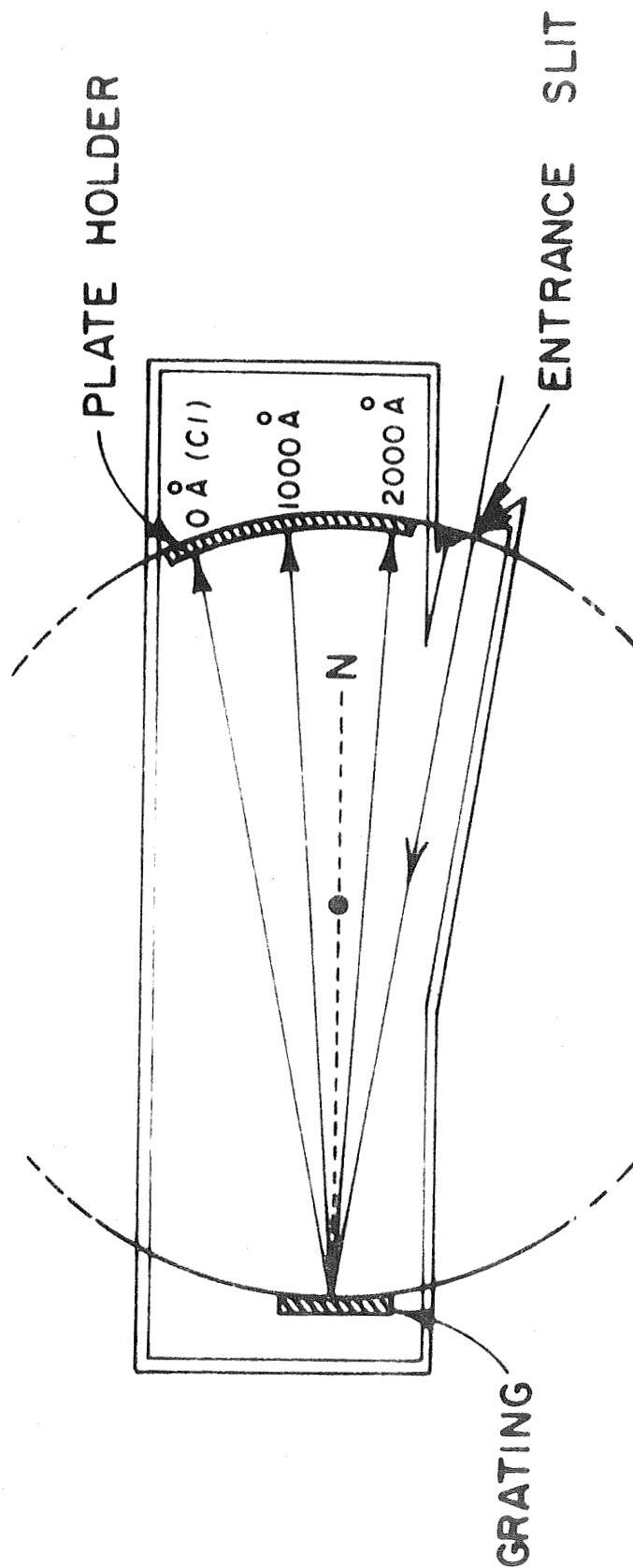


FIGURE 19 An optical configuration of a normal incidence spectrograph. The housing geometry is shown to illustrate the compact nature of this configuration. The dotted portions represent extension of Rowland circle.



in the figure lie on the Rowland circle so as to achieve sufficiently good focus for an extended wavelength region. An existing prototype for the present application has been designed, fabricated, and calibrated by McPherson Instrument Co. (a division of GCA Corporation) and utilized in a variety of rocket experiments designed to obtain vacuum ultraviolet spectra in the earth upper atmosphere is shown in Figure 20. A technique of stacking the two module assemblies for compactness is also illustrated in the figure. Further details of the basic spectrograph instrument are not included herein since these are available in the literature.<sup>(111)</sup> The recommended optical configuration involves overall unit assembly spectrograph dimensions of 4 inches depth by 8 inches width by 10 inches length (i.e.,  $320 \text{ in}^3$ ) with a weight of less than 5 lbs/instrument. Finally, it can be seen from the schematic of Figure 20 that the option is available to incorporate either a single spectrograph or the dual instrument on any specific Apollo mission.

The critical instrumental parameters are listed in Table 14 for both spectrograph designs wherein the indicated values have been assigned tentatively on the basis of a preliminary analysis of the present problem. It should be stressed at this point that all of the parametric requirements stipulated in this tabulation can be accommodated by off-the-shelf and state-of-the-art components. Brief discussions are presented below of the individual parameters included in Table 14 for both instrumental designs.

The indicated gratings are available from Bausch and Lomb<sup>(112)</sup> and other suppliers. The overall instrumental transmissivity estimate of 0.5

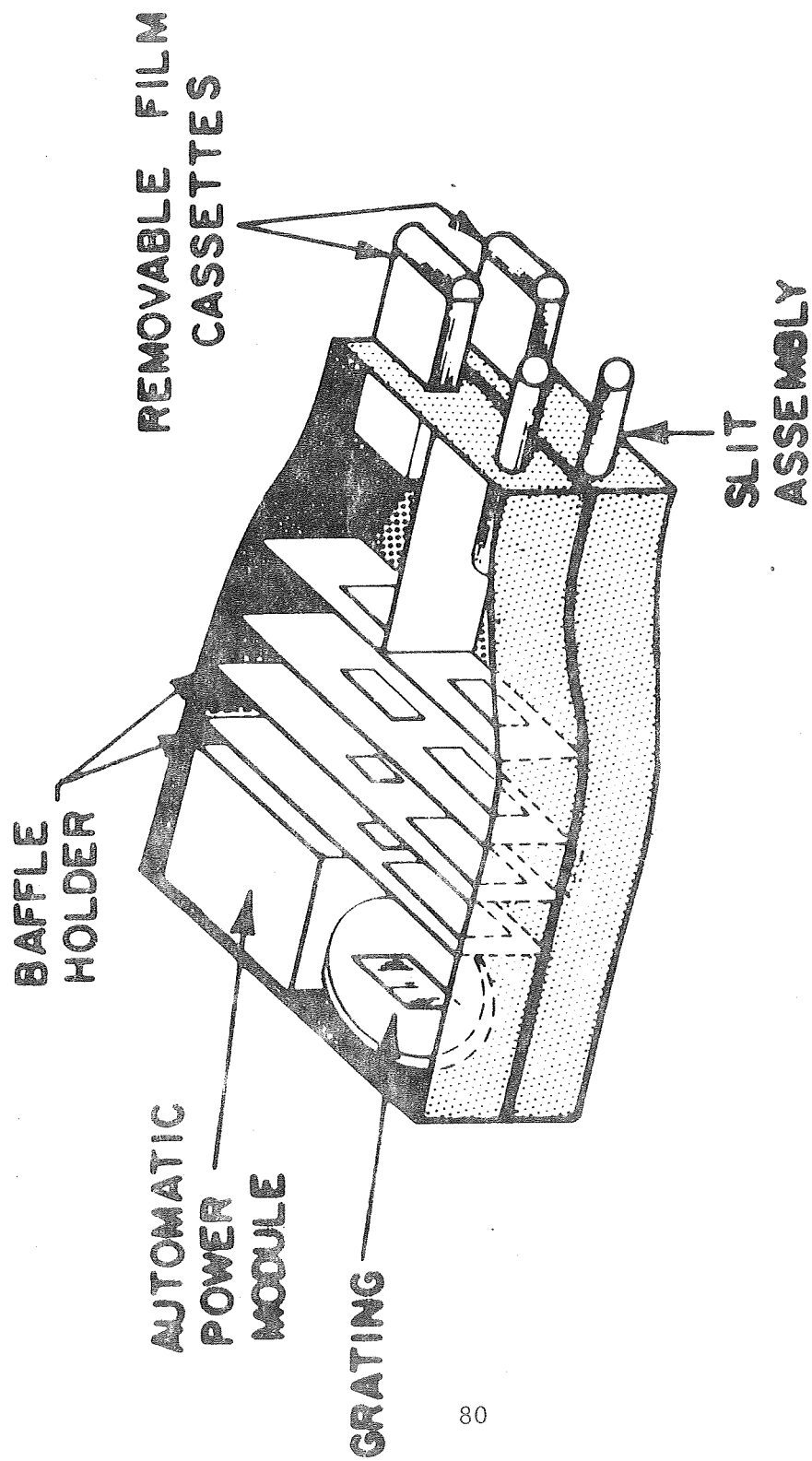


FIGURE 20 Detailed drawing of existing prototype. The overall dimensions are 4 x 8 x 10 inches

TABLE 14

## INSTRUMENTAL PARAMETERS FOR PORTABLE SPECTROGRAPHS

	Spectrograph #1 <u><math>\lambda\lambda</math> 2500-4500<math>\text{\AA}</math></u>	Spectrograph #2 <u><math>\lambda\lambda</math> 500-2500<math>\text{\AA}</math></u>
<u>Optical Specifications</u>		
Grating Specifications		
Grating Type	Concave blazed reflecting	Concave blazed reflecting
Focal Length, cm	20	20
Grating blaze, $\text{\AA}$	3200 (first order)	1200 (first order) 600 (second order)
Grooves/mm	1200	1200
Ruled area, mm	53 x 56	53 x 56
Reciprocal dispersion $\text{\AA}/\text{mm}$	$\sim 40$	$\sim 40$
Omega, $\Omega$ , steradians ( $\times 10^2$ )	7.4 (FOV $\sim 15^\circ$ )	7.4 (FOV $\sim 15^\circ$ )
Slit width, cm	0.10	0.10
Slit length, cm	1.0	1.0
Overall Transmissivity	0.5	0.5
<u>Film Specifications</u>		
Type	Kodak 2485	Kodak 101-01
Wavelength sensitivity, $\text{\AA}$	2200-6700	50-4000
Exposure Required for minimum density E, $\text{ergs}/\text{cm}^2$ ( $\times 10^4$ )	5.0	4.2
Mean E value, photons/ $\text{cm}^2$ ( $\times 10^{-7}$ )	8.0 ( $\lambda = 3200\text{\AA}$ )	2.5 ( $\lambda = 1200\text{\AA}$ )
Reciprocity Failure	Negligible	Negligible
Availability	Roll Form	Roll Form
<u>Instrument Overall Specifications</u>		
Size, inches	4 x 8 x 10	4 x 8 x 10
Weight, lbs.	5	5
Power requirements	None	None
Data measurements requirements	None	None
Data support requirements	None	None

for  $\lambda$  2500 to 4500Å is considered conservative owing to the high reflectivity of materials and grating efficiencies of this spectral region. Alternatively, for the spectral region  $\lambda < 1500\text{Å}$ , it is well-established<sup>(112)</sup> that reflectivities can be enhanced significantly by employing stock item platinum coated gratings which have been over-coated with magnesium fluoride. Therefore, an overall transmissivity of 0.5 was selected throughout the entire spectral region for the purposes of the present discussion. In practice, it is planned to establish the transmissivities of the individual spectrographs on the basis of a laboratory measurement program.

The rationale for the film selections of Table 14<sup>10</sup> can be discussed in terms of Figures 21, 22, and 23. Specifically for  $\lambda$  2500 to 4500Å Kodak 2485 film was selected on the basis of the spectral sensitivity curves of Figure 21, which was extracted directly from the appropriate Kodak data sheet. These published data were employed to obtain the corresponding E-values shown in Table 14. In the present experimental mode, it can be anticipated that relatively long exposure times may be involved so that the role of reciprocity failure must be considered. In this regard, it should be stressed that Lewis and James<sup>(113)</sup> have concluded recently that reciprocity failure was negligible when the film was employed under vacuum conditions. The resultant behavior is summarized in Figure 22 which was extracted directly from the cited paper. In addition, the results of the figure indicate that an increase in sensitivity occurs under vacuum conditions although this conclusion should be considered tentative. In any case, for the present purposes reciprocity

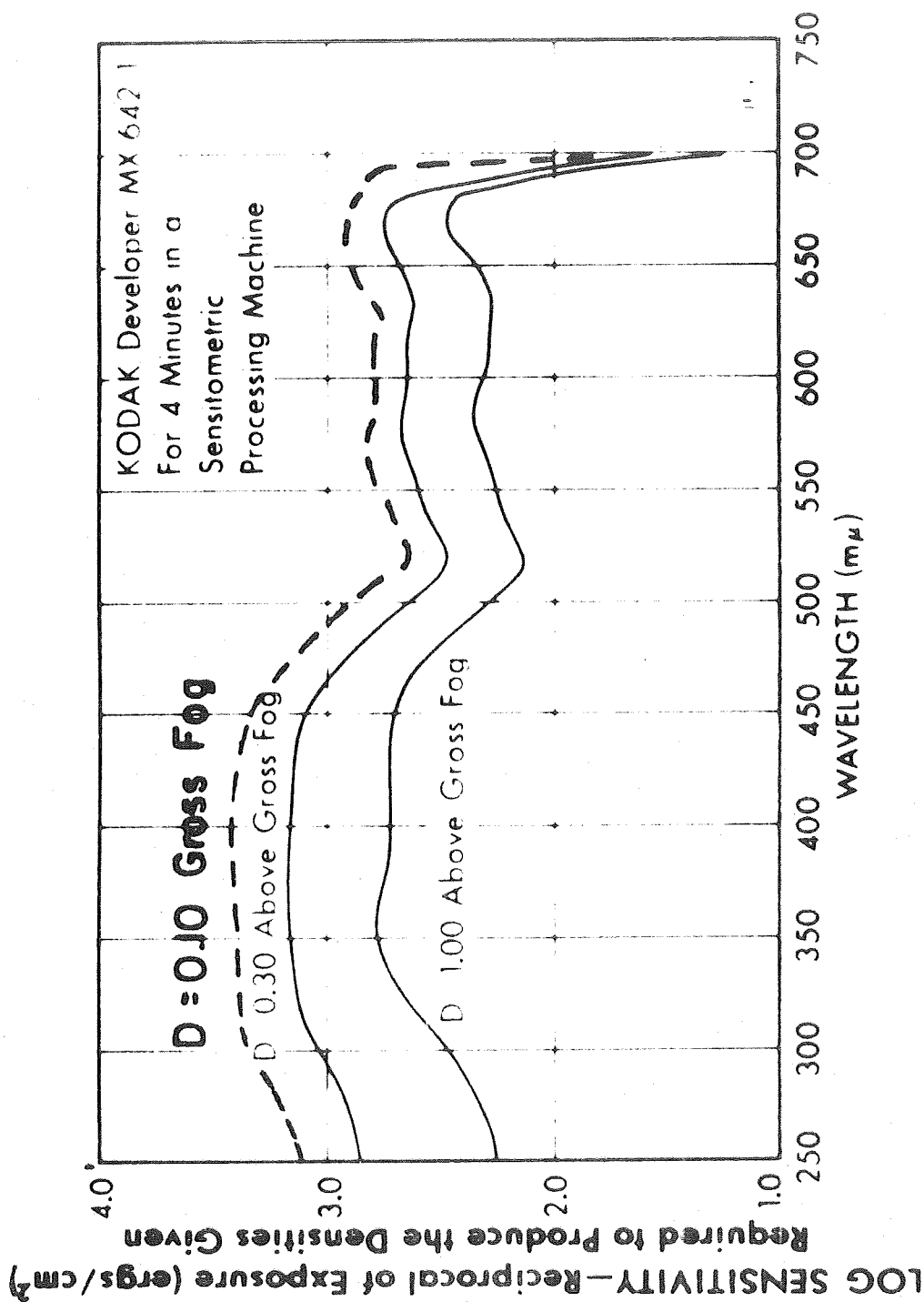


FIGURE 21 Spectral sensitivity of Kodak 2485 high speed recording film. The dotted curve obtains for  $D = 0.10$ .

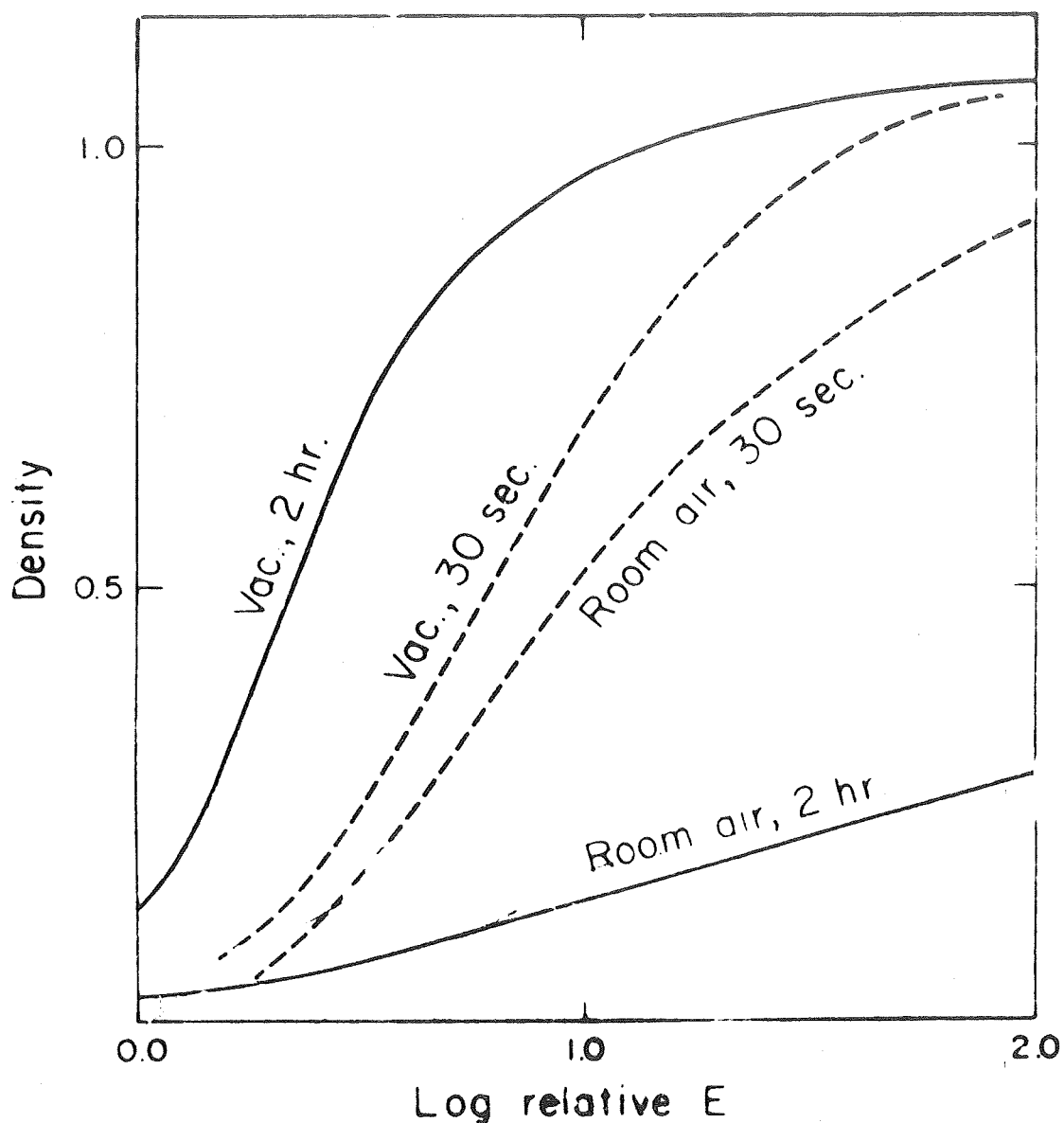


FIGURE 22

**Characteristic curves**  
for blue light exposure in room  
air and vacuum of pure bromide  
emulsion without deliberate  
chemical sensitization. Expos-  
ure times are noted on each curve.

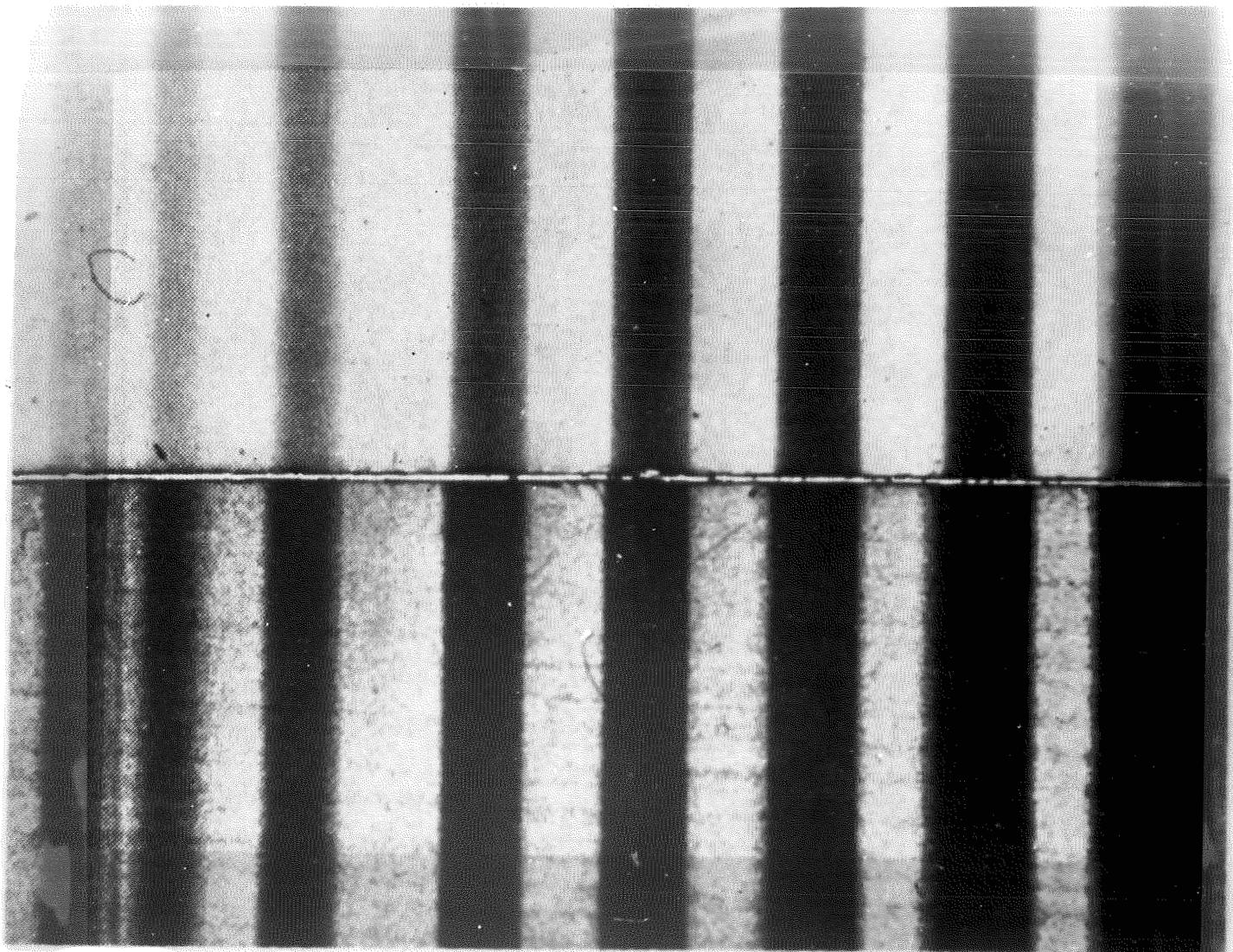


FIGURE 23 Series of exposures on SC-5 film at  $1200\text{\AA}$ . Exposure times were  $1/20$ ,  $1/10$ ,  $1/5$ ,  $1/2$ , 1, 2, 4, & 8 sec to a beam of  $1.7 \times 10^{-2}$  ergs/sec total flux. After exposure the film was cut in two and the upper half developed in DK-20 for 12 min while the lower half was developed in D-19b for 2 minutes.

failure was assumed to be negligible so that the sensitivity curves of Figure 21 are applicable for exposures up to about  $10^4$  seconds.

For the spectral region  $\lambda\lambda$  500 to  $2500\text{\AA}$ , the Kodak 101-01 film selection was predicated on the following rationale. An investigation was performed recently by W. K. Fowler, et al. <sup>(114)</sup> on the absolute calibration of SC-5 film employed for far ultraviolet rocket spectroscopy. A series of exposures of SC-5 film at a wavelength of  $1200\text{\AA}$  is shown in Figure 23 which has been extracted directly from the cited paper. <sup>(114)</sup> It can be seen that, even for an exposure time of 1/20 of one second and a beam intensity of  $1.7 \times 10^{-2}$  ergs/second, sufficient film exposure was obtained (for the indicated development process) as shown in the lower left slit image in Figure 23. On the basis of more recent experimental results, it is now recognized <sup>(115)</sup> that Kodak 101-01 film is both about 50 percent faster than the SC-5 film and also results in a clearer background upon proper development. Additionally, it has the further advantage of being available in roll form. On the basis of this increased capability, as well as the degree of darkening observed in the lower left slit image of Figure 23, estimates were derived for the exposure required for the minimum operating density of Kodak 101-01 film which are presented in Table 14. With respect to reciprocity failure, Fowler, et al. <sup>(114,115)</sup> have concluded that for SC-5 and 101-01 film, is completely negligible. Therefore, it is appropriate to apply the tabulated E-value to the calculation of exposure times required for the purposes of the present experiment.



It is suggested that the dual assembly spectrograph be operated within the protective shadow of the LEM. The optical axis of the instrument should be pointed about  $10^{\circ}$  above the lunar horizon with the slit oriented in the anti-solar position in order to minimize any degradation introduced by surface scattered radiation. This observational configuration can be instituted by the astronaut either by means of a built-in tripod arrangement or by simply suspending the dual spectrograph from a pre-selected location on the bottom section of the LEM vehicle. The astronaut would then initiate the instrumental operation mode wherein the entire sequence of pre-programmed exposures would be performed automatically through equipment shutdown (which occurs after several hours of operation). The only other required astronaut activity involves removal of the portable roll film holder for return to earth for subsequent film processing and data reduction and analysis. Thus, it is evident that although minimum astronaut activity is involved in the conduct of the proposed experiment, his role is vital to its successful performance.

As indicated previously, meaningful constituency data will be obtained for a system detectability of between 1 and 10 Rayleighs as shown in Table 13. On this basis then, a number of suggested exposure times have been selected employing the parametric instrumentation values discussed above and listed in Table 14. At this point, it is convenient to define the following useful parameters:

$X_B$  = the brightness value for the background radiation contained within the spectral resolution of one slit element. For convenience, this is given in units of Rayleighs (see Figure 24).

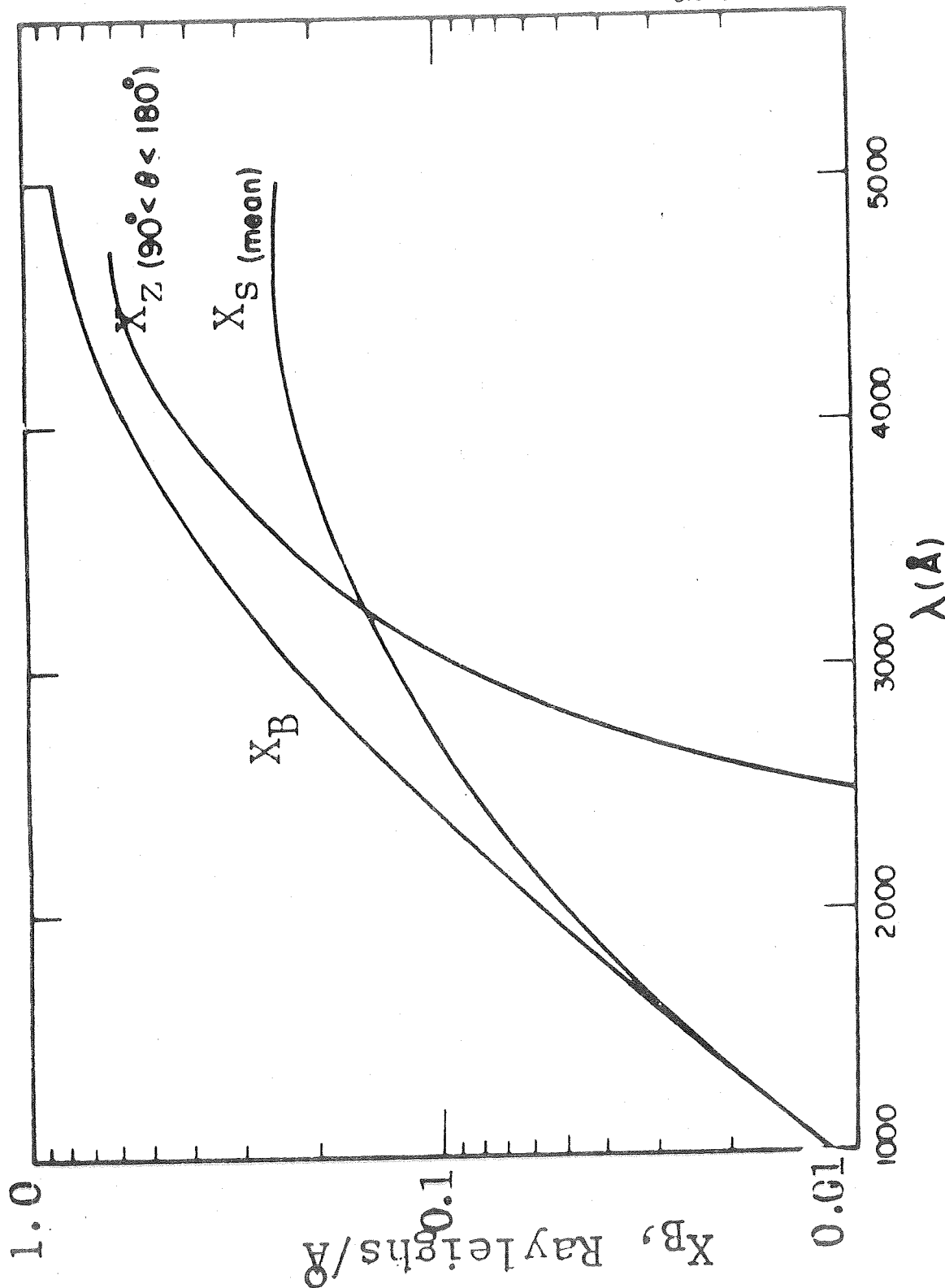


FIGURE 24 Total background intensity  $X_B = (X_S + X_Z)$  as a function of wavelength for mean galactic sky conditions and average elongation in the ecliptic ( $90^\circ < \theta < 180^\circ$ ).

- $X_s$  = the brightness for the spectrally discrete signals falling on the entrance slit. For convenience this is given in units of Rayleighs (see Table 13).  
 $A$  = slit area,  $\text{cm}^2$   
 $\Omega$  = viewing solid angle, steradians  
 $T$  = overall transmissivity, 0.50  
 $t$  = time of exposure, seconds  
 $\Phi$  = integrated exposure relevant to one slit area element image on photographic film,  $\text{ergs/cm}^2$ -slit area and/or photons/ $\text{cm}^2$ -slit area  
 $E$  =  $\Phi/A$ ; integrated exposure relevant to  $1 \text{ cm}^2$  image of photographic film (see Figures 21 and 22).

It is appropriate now to evaluate the exposure times required to achieve a 1 to 10 Rayleigh detection capability. This can be estimated in the following manner:

$$\Phi = (A\Omega) T \frac{[(X_s + X_B) t]}{4\pi} \quad (11)$$

so that

$$E = \frac{\Omega T [(X_s + X_B) t]}{4\pi} \quad (12)$$

Substitution from Table 14 yields:

$$E = 3.0 \times 10^{-3} [(X_s + X_B) t] \quad (13)$$

Equation (11) is plotted in Figure 25 where E-values of between  $10^7$  and  $10^8$  photons/ $\text{cm}^2$  (see Table 14) are plotted as a function of exposure times (t) in the range between 10 and 300 minutes. For future reference, a number of selected  $(X_s + X_B)$ -values are included which range between 0.5 and 40 Rayleighs. On the basis of these data, the background data shown

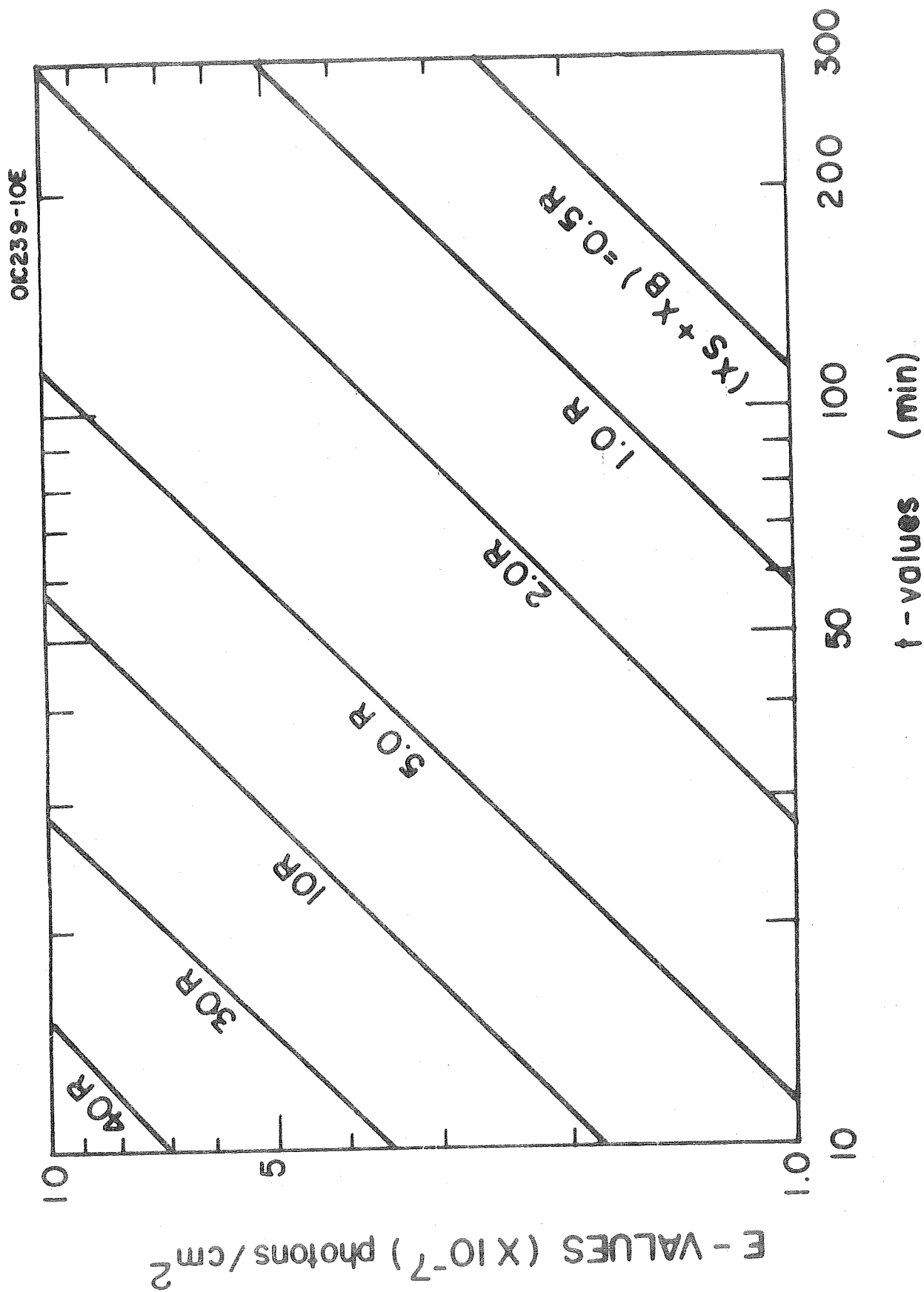


FIGURE 25 Plot of E-values in photons/cm<sup>2</sup> vs. t-values in minutes for a number of selected ( $X_s + X_B$ ) - values. These data can be employed to relate required exposure times to desired detectivity.

in Figure 24, and the instrumental characteristics listed in Table 14, it will be demonstrated that a 1-10 Rayleigh signal brightness detectability can be achieved by proper operation of the dual spectrograph on the lunar surface.

The results of Figure 25 demonstrate that the exposure time is selected on the basis of the anticipated  $(X_s + X_B)$ -value. It is important to stress here that the  $X_B$ -value is pertinent to the determination of the proper exposure time. Specifically, it is evident from the data in Figure 24 that the  $X_B$ -value exhibits significant variation over the spectral regions suggested for the two spectrograph instruments. Specifically, for  $\lambda\lambda$  2500-4500Å,  $X_B$ -values of between 4 and 40 Rayleighs (spectral resolution  $\sim 40\text{Å}$ ) obtain. Alternatively for the spectral region  $\lambda\lambda$  500-2500Å, the background contribution can be ignored for the most part. For this reason, exposure estimates are obtained individually for the two spectrograph systems.

With respect to  $\lambda\lambda$  2500-4500Å, a practicing rule of thumb of photography involves successful image detection against a strong background when the brightness of the image amounts to at least 10 percent of the background, i.e.  $(X_s + X_B)/X_B \geq 1.1$ . However, this rule prevails for photographic systems operating on the straight portion of the film gamma curve. This is illustrated in Figure 26 where  $X_s = X_B$  for which the resultant discrimination of signal against background is readily apparent. Owing to the lack of relevant information on the gamma curves of the presently considered film systems, a conservative approach is adopted wherein it is assumed that spectral discrimination can be achieved when

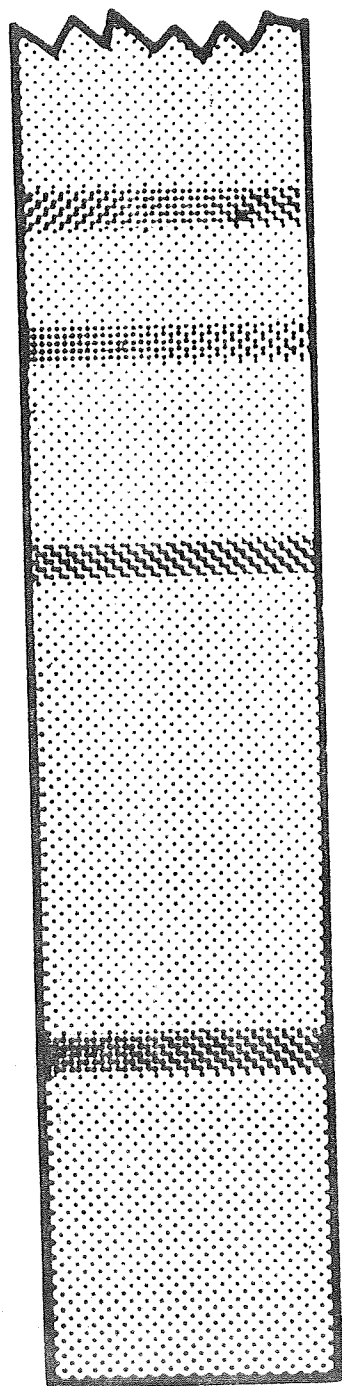


FIGURE 26 Schematic of typical photographic spectra wherein the signal and background film densities are equal.

$(X_s + X_B)/X_B \geq 1.25$ . On this basis, it is evident that proper exposure time selection must be predicated on the basis of the magnitude of the applicable background brightness rather than the signal brightness for  $\lambda\lambda$  2500-4500Å. Thus, according to Figure 25, for an E-value of  $8.0 \times 10^7$  photons/cm<sup>2</sup> presented in Table 14, exposure times of between 10 and 100 minutes are required for  $X_B$ -values of 40-4 Rayleighs, respectively. According to the detection criterion discussed above, a corresponding signal detection capability would be realized of between 10 and 1 Rayleigh, respectively. As a consequence, a recommended program of exposures would be employed in practice which includes exposure times of 1-300 minutes.

In contrast to the above situation, the spectral region  $\lambda\lambda$  500-2500Å involve no significant background contributions according to Figure 24. For this case, exposure time selection is predicated only on the basis of the magnitudes of the expected  $X_s$ -values. In this regard, the data of Figure 25 suggest that for the derived E-value of  $2.5 \times 10^7$  photons/cm<sup>2</sup> similar exposure times as those derived above for the  $\lambda\lambda$  2500-4500Å spectral region obtain for a 1-10 Rayleigh signal detection capability for the  $\lambda\lambda$  500 to 2500Å spectral region. Accordingly, it is recommended that an exposure time sequence identical to that obtained previously for  $\lambda\lambda$  2500-4500Å of between 10 and 300 minutes be selected for this lower spectral region.

Relevant to the above discussion, it may be noted that a well-established practice involves the controlled pre-exposure (to threshold) of fast film in order to enhance its speed characteristics.

The above suggested exposure time sequences should be regarded as tentative estimates since the final selection will be determined both on the basis of the specific prevalent background conditions as well as laboratory calibration of the optical components and films in the individual spectrograph systems. In this regard, an alternative instrumental configuration which would involve the employment of image intensification has not been considered herein owing to the additional instrumental complexities which would be introduced. However, in the event that such lower exposure times are necessary, this alternative could be applied to this experiment.

The photographic spectra obtained in the conduct of the proposed experiment require minimum analysis, since the film format intrinsically yields the unambiguous spectral locations of resonance scattering of the individual species. Alternatively, detailed interpretation of these results is expected to involve a considerable effort. For example, it is anticipated that the explanation of positive results will involve a detailed investigation to identify the major processes contributing to the existence of specific species in the lunar atmosphere. In addition, any measured time variation of the content of a given species will involve the identification of specific phenomenological sink and source functions such as solar wind activity, meteoric impact, LEM fuel contaminants, etc. It should be emphasized, however, that even negative results can be employed to establish meaningful upper limit values for a large number and variety of possible lunar atmospheric constituents. These data can then be utilized to preclude or evaluate the roles of several suggested



mechanisms contributing to the lunar atmosphere. Finally, the overall experimental results can be employed to evaluate the validity and feasibility of establishing a permanent astronomical-airglow lunar surface station to monitor selected lunar atmospheric species and communicate these data routinely to earth.

Successful performance of the proposed experiment would be assisted greatly by the performance of parallel, theoretical and laboratory investigations. The theoretical effort should involve an investigation of the relationship between specific lunar atmospheric species and appropriate source and sink functions as well as the mechanisms involved in generating steady-state concentrations. The laboratory investigation should involve the measurement of the optical characteristics of the two suggested spectrograph systems as well as absolute calibration of the films for employment herein. These supporting data would then be employed in the cogent interpretation of the derived experimental results.

### III. TECHNICAL PAPERS PRESENTED AT SCIENTIFIC AND/OR PROFESSIONAL MEETINGS

At the First Annual Meeting of the Division of Electron and Atomic Physics of the American Physical Society on 17-19 November 1969 a paper entitled "Angular Distributions of Photoelectrons and Partial Photoionization Cross Sections" was given by Dr. James A. R. Samson of GCA Technology Division, Bedford, Massachusetts. An experimental arrangement was given for measuring the angular distribution of photoelectrons. The asymmetry coefficient,  $\beta$ , was found to be 0.3 for argon, and 0.3 and 0.12 for molecular nitrogen at  $584\text{\AA}$  when the residual ion core is left in its  $X\ ^2\Sigma$  and  $A\ ^2\Pi$  states, respectively. The partial photoionization cross sections were given for  $O_2$  at 186, 209, 247, 330 and  $460\text{\AA}$ . New ionization potentials for  $O_2$  were found at 23.5, 24.6 and 27.3 eV  $\pm$  0.3 eV.

IV. QUARTERLY PROGRESS REPORT FOR HOURS WORKED IN THE PERIOD 1 SEPTEMBER 1969 THROUGH 24 NOVEMBER 1969

In compliance with the requirements of the subject contract, the following is an integrated tabulation of total hours worked by labor category and grade

Labor Category	Labor Grade	Total Hours
*Junior Technician	2	--
*Technician Experimental Machinist	3	219
*Senior Technician Senior Experimental Machinist	4	8
*Junior Scientist Junior Engineer	5	--
*Scientist Engineer	6	--
Senior Scientist Senior Engineer	7	--
Staff Scientist	8	--
Principal Scientist	9	156
Group Scientist Group Engineer	10	483

\*and other equivalent categories

Quarterly Total.....866

# REFERENCES

1. Baker, A. D., May, D. P. and Turner, D. W., J. Chem. Soc. (B) 22 (1968)
2. Clark, I. D. and Frost, D. C., J. Am. Chem. Soc. 89, 244 (1967).
3. Al-Joboury, M. I. and Turner, D. W., J. Chem. Soc. 4434 (1964).
4. Wilkinson, P. G., Can. J. Phys. 34, 596 (1956).
5. El-Sayed, M. F. A., Kasha, M. and Tanaka, Y., J. Chem. Phys. 34, 334 (1961)
6. Schulman, J. M. and Moskowitz, J. W., J. Chem. Phys. 43, 3287 (1965)
7. Hoffmann, R., J. Chem. Phys. 39, 1397 (1963).
8. Newton, M. D., Boer, F. P. and Lipscomb, W. N., J. Am. Chem. Soc. 88, 2367 (1966).
9. Dewar, M. J. S. and Klopman, G., J. Am. Chem. Soc. 89, 3089 (1967).
10. Momigny, J., Goffart, C. and D'Or, L., J. Mass Spectry. Ion Phys. 1, 53 (1968).
11. Natalis, P., Collin, J. E. and Momigny, J., J. Mass Spectry. Ion Phys. 1, 327 (1968).
12. Peatman, W. B., Borne, T. B. and Schlag, E. W., Proc. VI Intern. Conf. Phys. Electronic. and Atomic Collisions, Cambridge, 204 (1969)
13. Baker, A. D., Brundle, C. R., and Turner, D. W., J. Mass Spectry. Ion Phys. 1, 443 (1968).
14. Watanabe, K., J. Chem. Phys. 26, 542 (1957).
15. Watanabe, K., Nakayama, T. and Mottl, J., J. Quant. Spectrosc. Radiat. Transfer, 2, 369 (1962).
16. Person, J. C., J. Chem. Phys. 43, 2553 (1965).
17. Akopyan, M. E. and Vilesov, F. I., Khimiya Vysokikh Energii 2, 107 (1968). English translation in High Energy Chemistry, 2, 89 (1968).
18. Dibeler, V. H. and Rees, R. M., J. Res. Nat. Bur. Stand. 68A, 409 (1964).
19. Brehm, B., Naturforsch. 21a, 196 (1966).
20. Samson, J. A. R., Proc. Roy. Soc. (to be published).

21. Doolittle, P. H. and Schoen, R. I., Phys. Rev. Letters 14, 348 (1965)
22. Samson, J. A. R. unpublished data taken with 0.5Å resolution. See also the results of Akopyan and Vilesov in ref. 16.
23. Momigny, J. and Lorquet, J. C., Chem. Phys. Letters 1, 505 (1968).
24. Vilesov, F. I. and Akopyan, M. E. in "Elementary Photoprocesses in Molecules" (Akademia Nauk SSSR, Moskwa, 1966, English translation Plenum Press, New York, 1968) pp. 22.
25. Samson, J. A. R., "Techniques of Vacuum Ultraviolet Spectroscopy," (John Wiley & Sons, New York, 1967) pps. 142 and 154.
26. Mitchell, P. and Wilson, M. Chem. Phys. Letters 3, 389 (1969).
27. Cairns, R. B., Harrison, H. and Schoen, R. I., Appl. Optics (accepted for publication).
28. Samson, J. A. R. and Cairns, R. B., Phys. Rev. 173, 80 (1968).
29. Lindholm, E. and Jonsson, B. O., Chem. Phys. Letters 1, 503 (1967).
30. Jonsson, B. O. and Lindholm, E., Arkiv Fysik 39, 65 (1969).
31. Heddle, D. W. P., Jennings, R. E. and Parsons, A. S. L., J. Opt. Soc. Am. 53, 840 (1963).
32. Gill, P. and Heddle, D. W. O., J. Opt. Soc. Am. 53, 847 (1963).
33. Shardanand and Mikawa, Y., J. Quant. Spectrosc. Radiat. Trans. 7, 605 (1967).
34. Chaschina, G. I., Gladushchak, V. I. and Shreider, E. Ya., Optics and Spectroscopy 24, 542 (1968).
35. Dalgarno, A., Kingston, A. E., Proc. Roy. Soc. (London) A259, 424 (1961).
36. Kingston, A. E., J. Opt. Soc. Am. 54, 1145 (1964).
37. Liggett, G. and Levinger, J. S., J. Opt. Soc. Am. 58, 109 (1968).
38. Larsen, T. dissertation 1939, (Gleerupska Universit  t-Bokhandeln, Lund, Sweden).
39. Chan, Y. M. and Dalgarno, A., Proc. Phys. Soc. (London) 85, 227 (1965).
40. Hirschfelder, J. O., Curtiss, C. F. and Bird, R. B., Molecular Theory of Gases and Liquids, John Wiley and Sons, New York (Second Printing, corrected, with notes added, March, 1964).

41. Shardanand, J. Quant. Spectrosc. & Radiat. Trans. 8, 1373 (1968).
42. Rabinovitch, K., Canfield, L. R. and Madden, R. P., Appl. Optics 4, 1005 (1965).
43. Samson, J. A. R., J. Quant. Spectrosc. & Radiat. Trans. 9, 875 (1969).
44. Robbins, E. J. and Leckenby, R. E., Nature 206, 1253 (1965).
45. Poschenrieder, W. P. and P. Warneck, J. Appl. Phys. 37, 2812 (1966).
46. Poschenrieder, W. P. and Warneck, P., Anal. Chem. 40, 385 (1968).
47. Dibeler, V. H., M. Krauss, R. M. Reese, and F. N. Harlee, J. Chem. Phys. 45, 1287 (1966).
48. Chupka, W. A., J. Chem. Phys. 48, 2337 (1968).
49. Watanabe, K., T. Nakayama, J. Mottl, J. Quant. Spectry. Radiat. Transfer 2, 369 (1962).
50. Herzberg, G., Proc. Roy. Soc. (London) A262 (1961)
51. Matthews, C. S. and P. Warneck, J. Chem. Phys. 51, 854 (1969).
52. Haney, M. A. and J. L. Franklin, Trans. Faraday Soc. 65, 1794 (1969).
53. Skinner, H. A. (Private communication).
54. Kerv, J. A., Chem. Rev. 66, 465 (1966).
55. Marmo, F. F. and Warneck, P. Final Report Contract NASw-1283, GCA Technical Report No. 68-7-N.
56. Warneck, P. J. Chem. Phys. 46, 513 (1967).
57. Huxley, L. G. H. and Crompton, R. W. in Atomic and Molecular Processes, ed. D. R. Bates, Academic Press, New York (1962) p. 337.
58. Biondi, M. A. and Chanin, L. M., Phys. Rev. 94, 910 (1954).
59. Beaty, E. C., Proc. Fifth Int. Conf. on Ionization Phenomena in Gases (North Holland Publishing Co., Amsterdam, 1961).
60. McAfee, K. B., Sipler, D. and Edelson, D., Phys. Rev. 160, 130 (1967)
61. Madson, T. M. and Oskam, H. J. Physics Letters 25A, 407 (1967).
62. Saporoschenko, M. Phys. Rev. 139A, 352 (1965).
63. Keller, G. C., Martin, D. W. and McDaniel, E. W., Phys. Rev. 140A, 1535 (1965).

64. Ogawa, M. and Tanaka, Y., Can. J. Phys. 40, 1593 (1962).
56. Samson, J. A. R. and Weissler, G. W., Phys. Rev. 137A, 381 (1965).
66. Varney, R. N., Phys. Rev. 89, 708 (1953).
67. Kozyrev, N. A., Astrophys. Obs. Crimea 12, 169 (1954)
68. Polyakova, G. N., Fogel, Ya. M. and Mei, Ch'iu Yu, Soviet Astron. AJ. 7, 267 (1963)
69. Barth, C. A., Fastie, W. G., Hord, C. W., Pearce, J. B., Kelly, K. K., Stewart, A. I., Thomas, G. E., Anderson, G. P. and Raper, O. F., Science, 165, 1004 (1969).
70. Tanaka, Y., Jursa, A., & Le Blanc, F., J. Chem. Phys. 32, 1199 (1960)
71. Tanaka, Y. and Ogawa, M., Can. J. Phys. 40, 879 (1962).
72. Nakata, R. S., Watanabe, K. and Matsunaga, F. M., Science of Light 14, 54 (1965).
73. Cook, G., Metzger, P. and Agawa, M., J. Chem. Phys. 44, 2935 (1966)
74. Dibeler, V. H., and Walker, J. A., J. Opt. Soc. Amer. 57, 1007 (1967)
75. Cairns, R. B. and Samson, J. A. R., J. Geophys. Res. 70, 99 (1965)
76. Bahr, J. L. Blake, A. J., Carver, J. H. and Kumar, V., University of Adelaide report ADP 67 (1969)
77. Hinteregger, H. E., Annales de Geophys. (in press, 1970)
78. Schwenker, R. P, J. Chem. Phys. 42, 2618 (1965).
79. Anton, H., Ann. Physik, 18, 178 (1966).
80. Hesser, J. E., J. Chem. Phys. 48, 2518 (1968).
81. Hesser, J. E., and Dressler, K., J. Chem. Phys. 45, 3149 (1966).
82. Poulizac, M. C. and Dufay, M., Astrophys. Letters 1, 17 (1967).
83. Fjeldbo, G., Fjeldbo, W. C. and Eshlemen, V. R., J. Geophys. Res. 71, 2307 (1966).
84. Fjeldbo, G. and Eshleman, V. R., The Atmospheres of Mars and Venus. Edited by J. C. Brandt and M. B. McElroy (Gordon & Breach, 1968)
85. Fjeldbo, G., Kliore, A. and Seider, B., Radio Science (in press, 1969)

86. Kliore, A., Levy, G. S., Cain, D. L., Fjeldbo, G. and Rasool, S. I. Science, 158, 1683 (1967).
87. McElroy, M. B., J. Geophys. Res., 74, 29 (1969).
88. Green, A. E. S., and Barth, C. A., J. Geophys. Res. 72, 3975 (1967)
89. Dalgarno, A., McElroy, M. B. and Stewart, A. I., J. Atmos. Sci. 26, 753 (1969)
90. McConkey, J. W., Burns, D. J. and Woolsey, J. M., J. Phys. B. (Atom. Mol. Phys.) 1, 71 (1968).
91. Rapp, D. and Englander-Golden, P. G., J. Chem. Phys. 43, 1464 (1965)
92. Cloutier, P. A., McElroy, M. B. and Michel, F. C., J. Geophys. Res. 74 (in press)(1969)
93. Turner, D. W. and May, D. P., J. Chem. Phys. 46, 1156 (1967).
94. Spohr, R., and von Puttkamer, E., Z. Naturforsch. 22a, 705 (1967).
95. Sharp, T. E., and Rosenstock, H. M., J. Chem. Phys. 41, 3453 (1964).
96. Nishimura, H., J. Phys. Soc. (Japan) 21, 564 (1966).
97. Biondi, M. A., Can. J. Chem. 47, 1711 (1969).
98. Fite, W. L., Can. J. Chem. 47, 1797 (1969).
99. Sytinskaya, N. N., The Moon, edited by A. V. Markov, University of Chicago Press (1962).
100. Lyot, B. and Dollfus, A., Compt. Rend. Acad. Sci., Paris, 220, 1173 (1969)
101. Dollfus, A. Compt. Rend. Acad. Sci., Paris, 234, 2046 (1952).
102. Elsmore, B. Phil. Mag. 2, 1040 (1957).
103. Herzberg, G., Pop. Ast. 54, 414 (1946).
104. Kuiper, G. P., The Atmospheres of the Earth and Planets, edited by G. P. Kuiper, University of Chicago Press, Chicago (1952).
105. Marmo, F. F. and Engelman, A., Ann. of the N. Y. Acad. of Sci. 140, 69 (1966).



106. Marmo, F. F. and Manring, E., "Measured Maximum Abundances of Na I, Ca I and Ca II in the Lunar Atmosphere," The Moon (D. Reidel Publishing Company, submitted for publication).
107. Michel, F. C., "Interaction between the solar wind and the lunar atmosphere," Plan. Space Sci. 12, #11, 1075 (1964).
108. Mirtov, B. A., "Materials of the Lunar Surface in the Lunar Atmosphere," Geomagnetism i Aeron. 9, #1, 143 (1969).
109. Herzog, L. F., et al, "The Analysis of the Lunar Atmosphere by a Mass Spectroscope," Technical Report under Contract No. NASw-1480 (1968).
110. Hinten, F. L. and Taeusch, D. F., "Variation of the Lunar Atmosphere," J. Geophys. Res., 69, 1341 (1964).
111. Jursa, A., etals, "Nitric Oxide and Molecular Oxygen in the Earth's Upper Atmosphere," Planetary and Space Sci., 1, 161 (1959).
112. Certified Precision Diffraction Gratings, Bausch and Lomb (April, 1968)
113. Lewis, W. C. and James, T. H., "Effects of Evacuation on Low Intensity Reciprocity Failure and on Desensitization by Dyes," Photo. Sci. and Engineering, 13, #2, 54 (1969).
114. Fowler, W. K., Rense, W. A. and Simmons, W. R., "Film Calibration for Rocket Ultraviolet Spectrographs," Applied Optics, 4, #12, 1596 (1965).
115. Fowler, W. K. (private communication).